Oceanologia 64 (2022) 1—21

Available online at www.sciencedirect.com

ScienceDirect

journal homepage: www.journals.elsevier.com/oceanologia

ORIGINAL RESEARCH ARTICLE

Striped texture of submesoscale fields in the northeastern Baltic Proper: Results of very high-resolution modelling for summer season

Victor Zhurbas[a], **Germo Väli**[b,*], **Natalia Kuzmina**[a]

[a] *Shirshov Institute of Oceanology, Russian Academy of Sciences, Moscow, Russia*
[b] *Tallinn University of Technology, Tallinn, Estonia*

Received 22 May 2021; accepted 17 August 2021
Available online 28 August 2021

KEYWORDS
Baltic Sea;
Elongated submesoscale structures — stripes;
Modelling;
Symmetric instability;
McIntyre instability;
Frontogenesis;
Stirring

Abstract Very high-resolution modelling of the northeastern Baltic Proper shows that preferentially elongated along the flow, submesoscale inhomogeneities of hydrodynamic fields or stripes of the order of 10—20 km in length and 1 km in width, are typical for summer season both in surface mixed layer and for interior layers which are not directly exposed to atmospheric forcing. In surface layer, the presence of stripes is supported by the remote sensing imagery and their vertical extension is comparable with the mixed layer depth (approx. 5—8 m). In the interior layers, the vertical extension of stripes is considerably larger (approx. 10—50 m) and their slopes exceed the isopycnal slope. Four competitive mechanisms of formation of the mesoscale striped texture are considered: stirring of large-scale inhomogeneities by the eddy field, the classic, inviscid adiabatic fluid symmetric instability, the McIntyre instability, and the strain-induced frontogenesis. Based on the instability criteria and the growth rates and geometry of the disturbances, the classic symmetric instability and the strain-induced frontogenesis are probably responsible for the formation of submesoscale striped texture in the

* Corresponding author at: Department of Marine Systems, Tallinn University of Technology, Akadeemia tee 15A, 12618 Tallinn, Estonia.
E-mail address: germo.vali@taltech.ee (G. Väli).
Peer review under the responsibility of the Institute of Oceanology of the Polish Academy of Sciences.

Production and hosting by Elsevier

https://doi.org/10.1016/j.oceano.2021.08.003

surface layer, while in the interior layers, the strain-induced frontogenesis and hypothetically the McIntyre instability can be essential. Stirring of large-scale inhomogeneities by the eddy field could be responsible for formation of striped texture in a passive tracer concentration and in temperature and salinity in the presence of thermohaline gradients on isopycnic surfaces (thermoclinicity), but it does not imply formation of stripes in dynamically active tracers, such as vertical vorticity, horizontal gradients of buoyancy, etc.

1. Introduction

High resolution images of the sea surface both provided by remote sensing and simulated by very high-resolution circulation models display a variety of elongated submesoscale structures — thin filaments or stripes of the order of 1 km wide and 10—20 km long (e.g. Barkan et al., 2019; Brannigan et. al., 2017; Capet et al., 2008; Choi et al., 2017; D'Asaro et al., 2018; Gula et al., 2016; Jing et al., 2021; Karimova et al., 2012; McWilliams, 2016; Munk et al., 2000; Onken et al., 2020; Qiu et al., 2014; Schubert et al., 2020; Väli et al., 2017, 2018; Yu et al., 2019; Zhurbas et al., 2019a,b). Such elongated structures seem natural to associate with symmetric instabilities (SI) which are geometrically typified by overturning circulations about an axis aligned with the basic geostrophic flow — rolls (i.e. the disturbances are two-dimensional (2D) — they do not depend on the along-flow coordinate) (Bachman et al., 2017). The SI occurs in baroclinic flows when the Ertel potential vorticity q is opposite in sign of the Coriolis parameter f (Thomas et al., 2013):

$$fq < 0,\ q = (f\mathbf{k} + \nabla \times \mathbf{u}) \cdot \nabla b = q_{vert} + q_{bc}$$
$$q_{vert} = (f - u_y + v_x)b_z = \varsigma_{abs} b_z \qquad (1)$$
$$q_{bc} = (w_y - v_z)b_x + (u_z - w_x)b_y$$

Here $\mathbf{u}$ is the velocity, $\mathbf{k}$ is the vertical unit vector, $b = -g(\rho - \rho_0)/\rho_0$ is the buoyancy defined in terms of the gravitational acceleration g, potential density ρ and constant reference density ρ_0, $\varsigma_{abs} = f - u_y + v_x$ is the absolute vertical vorticity. In more detail, the instability condition $fq < 0$ implies a variety of instabilities such as (Bachman et al., 2017)

Gravitational instability: $b_z < 0$ (2)

Inertial instability: $f\varsigma_{abs} < 0, b_z > 0$ (3)

Symmetric instability:
$fq_{bc} < 0, |fq_{bc}| > fq_{vert},\ fq_{vert} > 0,\ b_z > 0$ (4)

If the flow is in geostrophic balance, we can apply the thermal wind relation ($u_z = -b_y/f$, $v_z = b_x/f$, $w = 0$) and rewrite the expression for q_{bc} in Eq. (1) as

$$q_{bc} = -(b_x^2 + b_y^2)/f \qquad (5)$$

and further the SI condition as (Haine and Marshall, 1998; Hoskins, 1974)

$$Ri\frac{\varsigma_{abs}}{f} = Ri(1 + Ro) < 1, Ro > -1, b_z > 0 \qquad (6)$$

where $Ri = N^2/(u_z^2 + v_z^2) = f^2N^2/(b_x^2 + b_y^2)$ is the geostrophic Richardson number, $Ro = (-u_y + v_x)/f$ is the gradient Rossby number defined as the ratio of vertical relative vorticity $\zeta = -u_y + v_x$ to the planetary vorticity f, and $N^2 = b_z$ is the buoyancy frequency squared.

Eq. (5) says that the baroclinicity of the fluid always works to reduce the potential vorticity and the SI occurs when the baroclinicity term q_{bc} of the Ertel potential vorticity q becomes prevalent over the vertical stratification and vorticity term q_{vert}. Such a prevalence is more likely to occur in the upper mixed layer where the vertical stratification is commonly weak and can be further weakened relative to the baroclinicity term that can increase due to atmospheric forcing (e.g. due to cross-front advection of dense water over light by Ekman transport driven by winds with down-front component (Thomas, 2005) — the situation that was revealed within the Northern Wall of the Gulf Stream (Thomas et al., 2013)).

The SI growth rate ω_i and horizontal lengthscale L can be estimated for constant shear and stratification (see Eq. (1.4), (2.28), and (2.29) of Stone (1966)) as

$$\omega_i = f\frac{\sqrt{1 - Ri}}{\sqrt{Ri}},\ L < 2\frac{U}{f}\sqrt{1 - Ri} \qquad (7)$$

where U is the velocity of the basic geostrophic flow. In accordance to Eq. (7), for typical ocean parameters, $U = 0.1$ m/s, $f = 1\bullet10^{-4}$ s^{-1}, and SI favoring condition, $Ri = 0.25$—0.95, the SI time ($1/\omega_i$) and length (L) scales are in the range of $(0.58$—$4.35)/f$ or 1.6—12 hours and below 0.45—1.7 km, respectively.

Favorable conditions for SI are also expected in the bottom boundary layer over sloping seabed where a cross-flow advection of dense water over light water by Ekman transport driven by bottom friction can reduce vertical stratification and increase baroclinicity (e.g. Garrett et al., 1993; Umlauf and Arneborg, 2009; Zhurbas et al., 2012).

The possibility to meet the SI condition Eq. (4) in well stratified interior layers of the sea that are not directly exposed to the atmospheric forcing and bottom friction seems questionable and should be additionally tested. However, one has to keep in mind that this instability condition is formulated in terms of the Ertel potential vorticity of inviscid adiabatic fluid and does not account for effects of vertical eddy viscosity and diffusion. If vertical eddy viscosity and diffusion is taken into account (see Eq. (3.3.a) and an unnumbered equation next to (3.5) in McIntyre (1970) and Appendix 1 for details), the SI condition Eq. (6) will change

for

$$Ri(1+Ro) < \frac{(1+Pr)^2}{4Pr}, Ro > -1,\ b_z > 0 \tag{8}$$

where Pr is the Prandtl number defined as the ratio of apparent vertical viscosity to diffusion of buoyancy. For this reason, diffusive destabilization of baroclinic geostrophic flow relative to 2D (symmetric) disturbances at $1 \le Ri < (1+Pr)^2/(4Pr)$ is referred as the McIntyre instability (Ruddick, 1992). In stratified ocean the Pr value can be much larger than 1 because e.g. the low (near-inertial) frequency internal waves (Lappe and Umlauf, 2016; Thomas et al., 2016) can effectively contribute to the vertical transport of momentum without contributing to the vertical transport of mass/buoyancy. Comparing growth rates of symmetric disturbances in viscous non-adiabatic and inviscid adiabatic cases, the corresponding inviscid adiabatic modes usually have the numerically highest growth rates (McIntyre, 1970).

Apart from the diffusive destabilization, the baroclinic geostrophic flow in the ocean is subject to double-diffusive destabilization relative to 2D (symmetric) disturbances Kuzmina and Rodionov, 1992; Kuzmina and Zhurbas, 2000; May and Kelley, 1997) caused by the differences in vertical apparent diffusivities for scalar quantities that determine the sea water density/buoyancy – temperature and salinity, in accordance with parameterization by Stern (1967). Therefore, there are at least three types of symmetric instability of baroclinic geostrophic flows: classic or inviscid adiabatic SI (SI), diffusive SI (DSI or McIntyre instability), and double-diffusive SI (DDSI). The DSI can exist at a wider range of Ri than SI (cf. Eq. (6) and (8) while DDSI is possible at any large value of Ri (Kuzmina and Zhurbas, 2000). The maximum growing SI disturbance is aligned to the isopycnal slope and gains the kinetic energy (KE) from the mean sheared flow, while the submesoscale and mesoscale currents/eddies gain KE primarily through the release of available potential energy stored in baroclinic fluid (Thomas et al. 2013, 2016). In contrast to SI, the maximum growing DSI and DDSI disturbances at $Pr > 1$ have a smaller slope than the isopycnal slope and gain KE through the release of available potential energy of baroclinic fluid (Kuzmina and Zhurbas, 2000; McIntyre 1970). The SI, DSI and DDSI are characterized not only by different Ri ranges, but also by different growth timescales: the timescales for DSI and DDSI are larger than the timescale for SI (Kuzmina and Zhurbas, 2000; McIntyre, 1970; see also Appendix 1).

Apart from the symmetric instabilities, the elongated submesoscale features seen in the horizontal plane view of the vertical vorticity, temperature, material concentration c, etc. can be generated by strain-induced frontogenesis (McWilliams, 2016; Munk et al., 2000). Frontogenesis is a classical dynamical process in meteorology (Hoskins and Bretherton, 1972; Hoskins, 1982) and ocean (Kuzmina, 1981; Macvean and Woods, 1980) where a background horizontal deformation flow such as $u_d = \alpha x,\ \ v_d = -\alpha y,\ \ w_d = 0,\ \alpha > 0$ with a uniform strain rate

$$\alpha = \left(\frac{\partial u_d}{\partial x} - \frac{\partial v_d}{\partial y}\right)/2 \tag{9}$$

provides a rapid growth of y-aligned surface horizontal gradients of buoyancy b_y, velocity u_y and passive tracer concentration, c_y. The growth is exponential for passive tracer ($c_y \sim \exp(\alpha t)$) and can be even super-exponential for the dynamically active b (Hoskins and Bretherton, 1972; Hoskins, 1982). In the course of strain-induced frontogenesis in inviscid adiabatic fluid, the frontal jet symmetry is violated towards a strong cyclonic shear and a weak anticyclonic shear: at time $2.5\alpha^{-1}$ the associated Rossby numbers are $Ro^+ = 1$ and $Ro^- = -0.3$, respectively. Soon afterwards, at $2.89\alpha^{-1}$, the singularity is achieved with $Ro^+ = +\infty$ while the anticyclonic shear remains at $Ro^- = -0.3$ (Macvean and Woods, 1980; Munk 2001; Ou, 1984). Remarkable that the modelled filamentous submesoscale features in the surface ocean layer are characterized by very high cyclonic shear at $Ro > 1$ (McWilliams, 2016; Onken et al., 2020; Väli et al. 2017). In context of filamentous submesoscale features, the primary background strain can be from mesoscale currents and eddies as well as from submesoscale coherent vortices, while the seed buoyancy gradients are created either by the quasigeostrophic chaotic advection of the mesoscale b field or by the mixed layer instabilities (McWilliams, 2016).

In the general case the horizontal strain rate is defined as (e.g. Gula et al. (2014))

$$S = \sqrt{(u_x - v_y)^2 + (v_x + u_y)^2} \tag{10}$$

The principal strain axis, given by the angle θ_p such that

$$\tan(2\theta_p) = \frac{v_x + u_y}{u_x - v_y} \tag{11}$$

corresponds to the direction of the maximum stretching, while its perpendicular direction corresponds to the maximum contraction. The straining will induce frontogenesis if the principal strain axis is aligned with the axis of the front. There is a link between the strain-induced frontogenesis and SI, namely, the enhancement of lateral buoyancy gradients due to frontogenesis in conjunction with atmospheric forced surface buoyancy loss can produce a negative Ertel potential vorticity q and thereby trigger SI (Jing et al., 2021).

There is another possibility of the striped texture formation, which can be considered as a null hypothesis. This refers to stirring of large-scale inhomogeneities by the eddy field (e.g. Villermaux (2019)). Smith and Ferrari (2009) have shown that temperature and salinity filaments with slopes much steeper than the isopycnal slope can be generated through lateral stirring of large-scale thermohanine gradients on isopycnal surfaces (thermoclinicity) by a vigorous geostrophic eddy field developed through barocinic instability in the framework of a quasi-geostrophic model. Effect of stirring is demonstrated in Appendix 2 where the evolution of a constant gradient of the tracer concentration in a time-dependent, non-divergent 2D velocity field, consisting of two gyres that conversely expand and contract periodically in the x-direction, is considered. It is shown that for the advection time much longer than the period of eddy rotation and expansion-contraction, the constant gradient tracer concentration transforms into a striped texture, while the velocity and vorticity fields remain free of any strip-like irregularities.

Baltic Sea (Figure 1) is known for summer cyanobacteria blooming (e.g. Finni et al. (2001)) which provides outstanding ability to visualize filamentous submesoscale

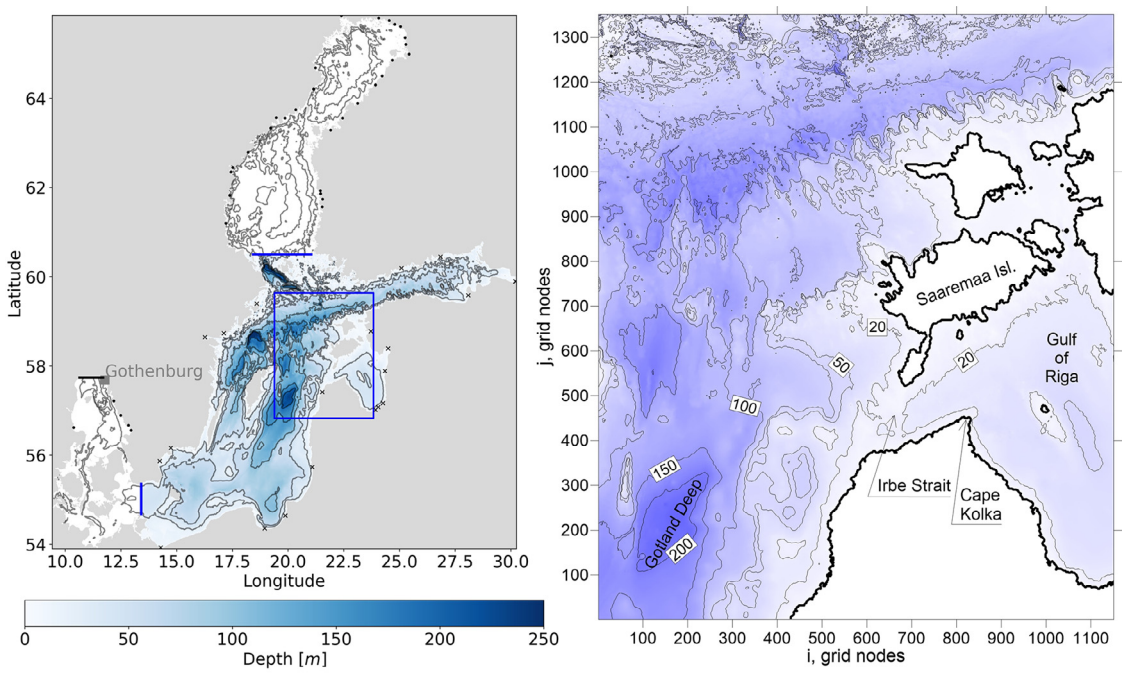

Figure 1 Bathymetric map of the Baltic Sea. Left panel: The high resolution model domain (filled colors) with the open boundary locations (bold blue lines). The coarse resolution model domain (blank contours + filled colors) has an open boundary close to Gothenburg (bold black line). Right panel: Close-up of the northeastern Baltic Proper (the study area). The river mouth locations in the coarse model setup and in both setups are marked with dots and crosses, respectively.

structures and coherent vortices in remote sensing optical images of the sea surface. Such images were even used in review articles to demonstrate submesoscale phenomena (e.g. McWilliams (2016)). Several attempts were done to reproduce submesoscale features seen on remote sensing images of the Baltic Sea using very high-resolution circulation models (Laanemets et al., 2011; Onken et al., 2020; Vankevich et al., 2016; Zhurbas et al., 2008; 2019a,b). Statistics of submesoscale coherent vortices simulated in the surface layer of the Baltic Sea was accessed in Vortmeyer-Kley et al. (2019). Rotation of floating particulate matter in submesoscale vortices and its aggregation into filamentous features was studied by means of numerical modelling of the Baltic Sea circulation (Giudici et al., 2021; Kalda et al., 2014; Väli et al., 2018; Zhurbas et al., 2019a,b). Diagnosis of mixed layer instabilities as applied to the surface layer of the Baltic Sea was performed by Onken et al. (2020) and Chrysagi et al. (2021) based on submesoscale simulations. In summer, the SI condition (Eq. (4)) was found to be satisfied in 1.8—4.8% of the grid cells in the surface layer of a 100 km × 100 km model domain to the south of the Bornholm Island (Onken et al., 2020). Negative values of the Ertel potential vorticity consistent with SI were found in the down-wind flank of a frontal filament emerged during a storm event in the Eastern Gotland Basin (Chrysagi et al., 2021). Seasonality of submesoscale coherent vortices in different layers of the Baltic Sea was addressed in Väli and Zhurbas (2021) based on very high-resolution modelling. Kuzmina et al. (2005) showed that DDSI was probably responsible for generation of thermohaline intrusions observed in the permanent halocline of the Eastern Gotland Basin after the 1993 Major Inflow.

Almost all of the above sited studies of submesoscale processes were focused on the surface mixed layer. Meanwhile, submesoscale processes are not limited to the surface mixed layer, where they are probably most intensive, but can also be active in the interior sea layers (McWilliams, 2016; Smith and Ferrari, 2009; Yu et al., 2019). The objective of this work is to simulate submesoscale flows typical for summer season in the northeastern Baltic Proper based on a very high-resolution circulation model, compare the submesoscale filaments of the surface layer with those in the interior layers, and provide diagnosis of formation mechanisms based on the above listed criteria.

2. Material and methods

2.1. Model description

The General Estuarine Transport Model (GETM) (Burchard and Bolding, 2002) was applied to simulate the meso- and submesoscale variability of temperature, salinity, currents, and overall dynamics in the northeastern Baltic Proper. GETM is a primitive equation, 3-dimensional, free surface, hydrostatic model with the embedded vertically adaptive coordinate scheme (Hofmeister et al., 2010) which reduces the artificial numerical mixing in the simulations (Gräwe et al., 2015). The vertical mixing is parametrized by two equation k-ε turbulence model coupled with an algebraic second-moment closure (Burchard and Bolding, 2001; Canuto et al., 2001). The implementation of the turbulence model is performed via General Ocean Turbulence Model (GOTM) (Umlauf and Burchard, 2005).

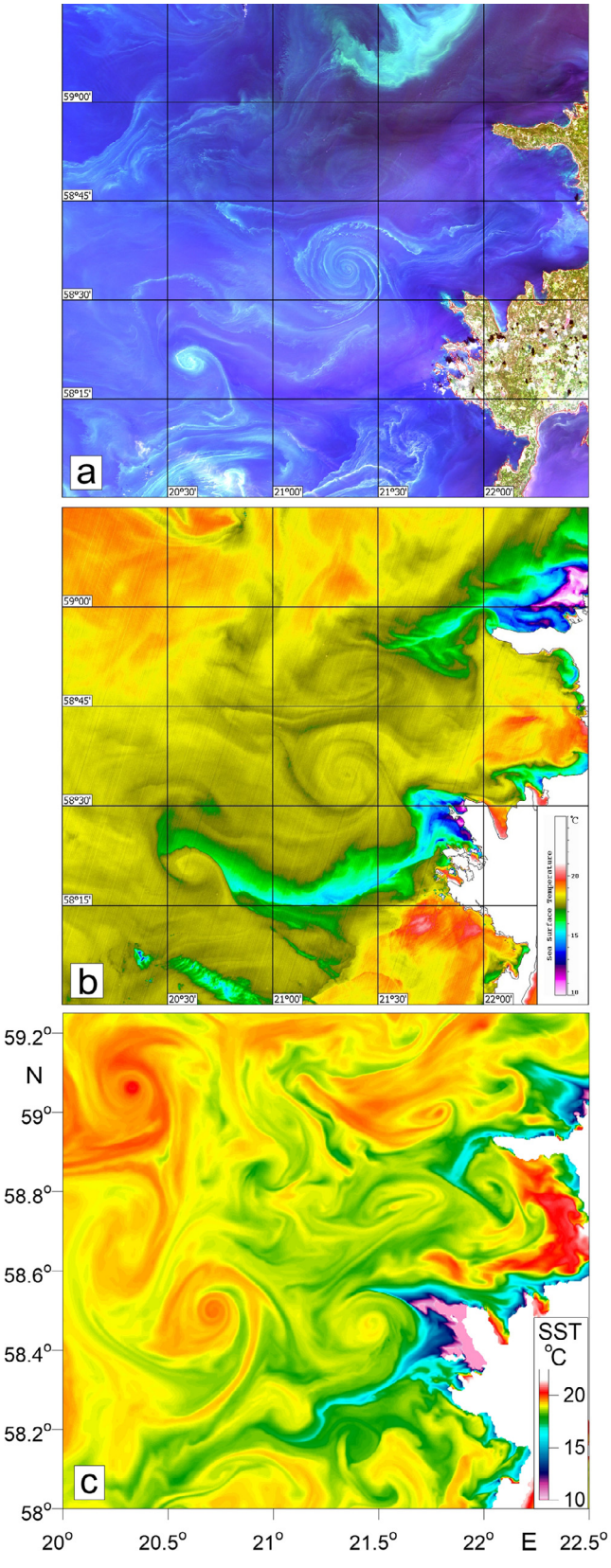

Figure 2 Colour snapshot (a) and infrared SST map (b) of an area west of the Moonsund from Operational Land Imager (OLI) and Thermal Infrared Sensor (TIRS) of the Landsat 8 satellite on 2018/07/18 19:00 UTC versus modelled SST (GETM, 0.125 NM grid) on 2018/07/18 07:07 UTC (c).

For the horizontal and vertical transport of momentum and tracers, a second-order total variation diminishing (TVD)-scheme with Superbee limiter with reduced spurious mixing (Klingbeil et al., 2014 and 2018) is applied.

The coarse resolution model covers the entire Baltic Sea with an open boundary in the Kattegat and has the horizontal resolution of 0.5 nautical miles (926 m) over the whole model domain. The coarse resolution model run is started from 1 April 2010 with initial thermohaline conditions taken from the Baltic Sea reanalysis for the 1989—2015 by the Copernicus Marine service. More detailed information about the model setups is available in Zhurbas et al. (2018 and 2019a) and for the coarse resolution model in Liblik et al. (2020).

The horizontal grid of the high-resolution nested model with uniform step of 0.125 nautical miles (approximately 232 m) all over the computational domain, which covers the central Baltic Sea along with the Gulf of Finland and Gulf of Riga (Figure 1), is applied while 60 adaptive layers in the vertical direction are used, and the cell thickness in the surface layer within the study area does not exceed 1.8 m. The digital topography of the Baltic Sea with the resolution of 500 m (approximately 0.25 nautical miles) is obtained from the Baltic Sea Bathymetry Database (http://data.bshc.pro/) and interpolated bi-linearly to 232 m resolution.

Nested model simulation run is performed from 1 April to 20 September 2018. The model domain has the western open boundary in the Arkona Basin and the northern open boundary at the entrance to the Bothnian Sea (see Figure 1 for details). For the open boundary conditions the one-way nesting approach is used and the coarse resolution model results along the open boundaries are utilized. Sea-level fluctuations with 1-hourly resolution and temperature, salinity and current velocity profiles with 3-hourly resolution are interpolated using the nearest neighbour method in space to the higher resolution grid. In addition, the profiles are vertically interpolated to 2 m resolution and extended to the bottom of the high resolution model. Flather (1994) radiation condition is used for the obtained sea-level fluctuation data and relaxation towards obtained profiles with sponge layer factors according to the method of Martinsen and Engedahl (1987) during simulations at the boundary.

The atmospheric forcing (the wind stress and surface heat flux components) is calculated with bulk formulae from the wind components, solar radiation, air temperature, total cloudiness and relative humidity data generated by the operational model HIRLAM (High Resolution Limited Area Model) maintained by the Estonian Weather Service with the spatial resolution of 11 km and temporal resolution of 1 hour (Männik and Merilain, 2007). The wind velocity components at the 10 m level along with other HIRLAM meteorological parameters are bi-linearly interpolated to the model grid.

The freshwater input from 54 largest Baltic Sea rivers together with their inter-annual variability is taken into account in the coarse resolution model. The original dataset consists of daily climatological values of discharge for each river, but inter-annual variability is added by adjusting the freshwater input to different basins of the sea to match the values reported annually by HELCOM (Johansson, 2018).

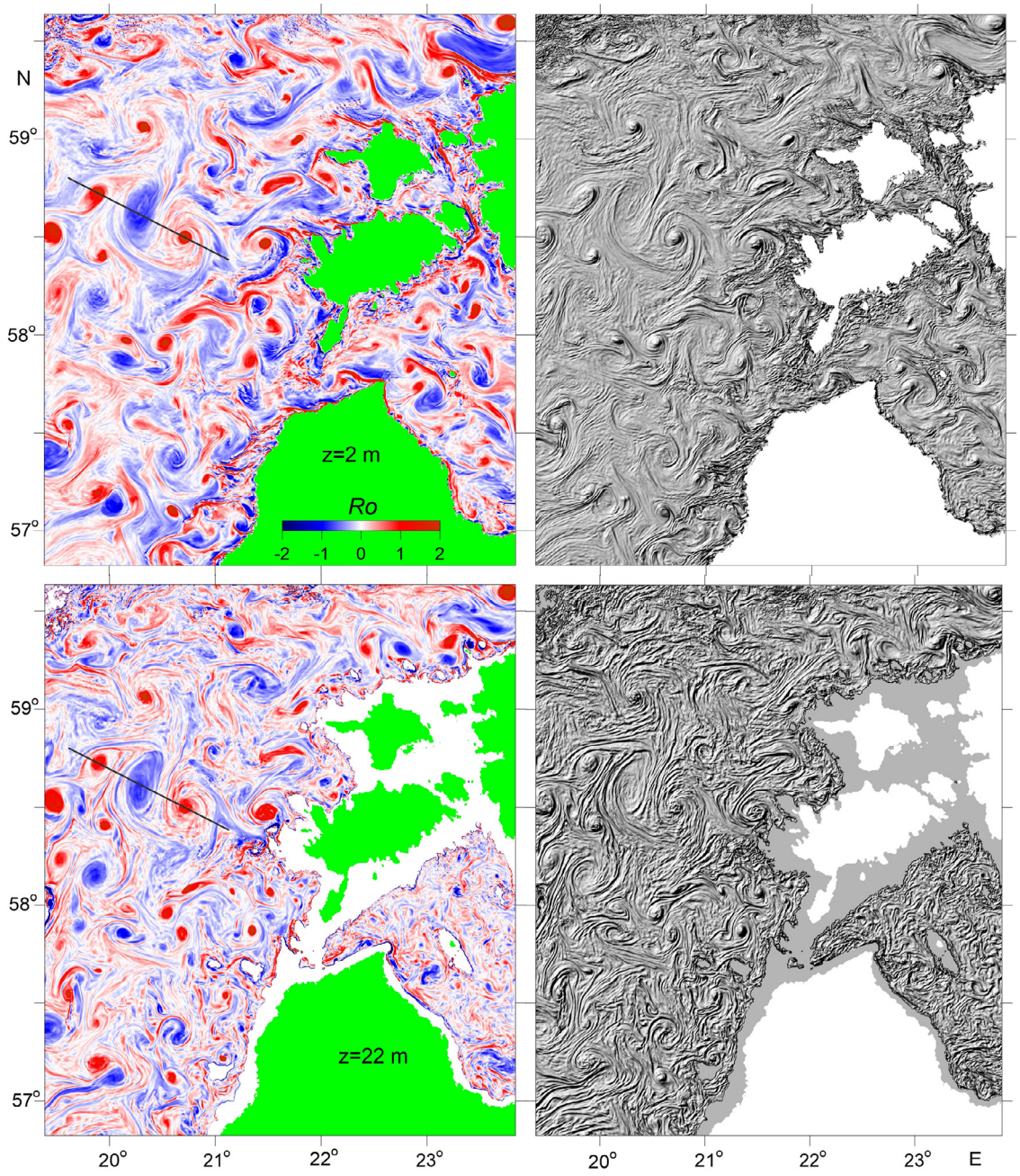

Figure 3 Left panels: gradient Rossby number $Ro = \varsigma / f$ simulated on 2018/7/18 07:07 UTC at 2 m (top) and 22 m (bottom) levels. A black line on the left panels is the location of a transect to be analyzed in Figure 5 and 12. Right panels are the same but in the shaded relief form to highlight the striped texture.

The initial temperature and salinity fields are obtained from the coarse resolution model for 1 April 2018 and interpolated using the nearest neighbour method to the high-resolution model grid. In addition, as the adaptive vertical coordinates are used in both setups, the T/S profiles from coarse resolution are linearly interpolated to fixed 10 m vertical resolution before interpolation to the high resolution and extended to the maximum depth of high-resolution model. The model runs are started from motionless state and zero sea surface elevation. The spin-up time of the Baltic Sea model under the atmospheric forcing is expected to be within 10 days (Krauss and Brügge, 1991; Lips et al., 2016), while the model output for comparison with the respective satellite imagery was obtained after 108 days of simulation.

2.2. Model validation

The coarse-resolution model (926 m grid), whose output was used as the initial and open boundary conditions in the nested, high-resolution model (232 m grid), has been thoroughly tested by means of comparison of the simulated and observed current velocity variance and timeseries of sea-level fluctuations, temperature and salinity in the surface, intermediate and bottom layers for a number of monitor-

ing stations of the Baltic Sea (see Zhurbas et al. (2018) for details).

The ability of the nested, high-resolution model to reproduce the observed submesoscale structures is demonstrated in Figure 2 where the optical and infrared sea surface temperature (SST) snapshots of an area west of the Saaremaa and Hiiumaa islands (Moonsund), Estonia, from Landsat-8 mission is presented versus the modelled SST for 2018/07/18. The snapshots were taken during the period of summer blooming of cyanobacteria, when the submesocale motions have assembled the phytoplankton material into filaments winded up into spirals thereby visualizing coherent submesoscale vortices. Note that the cyclonic vortices/spirals are visualized better than the anticyclonic ones which can be explained by larger rotation frequency and more pronounced differential rotation (Zhurbas et al., 2019b). Similar pattern of submesoscale filaments and eddies is seen in the simulated SST map; the difference is that the simulated pattern is more densely populated with submesoscale features in comparison to the remote sensing optical image which can be probably explained by the lack of visualizing tracer (phytoplankton) in some parts of the study area. The remote sensing SST is in good agreement with the modelled SST, displaying almost identical areas of pronounced coastal upwelling and many submesoscale eddies. Of course, one cannot expect that the model will reproduce the mutual arrangement of vortices in remote sensing images, since it is impossible to simulate the individual realization of a random process of the formation of submesoscale vortices.

3. Results

The simulated submesoscale filaments — stripes occurred to be found in different tracer fields not only in the surface layer but also in the interior layers. To illustrate this, we calculated patterns of the gradient Rossby number $Ro = \zeta / f$ (Figure 3) and the horizontal temperature gradient modulus $|\Delta_H T| = \sqrt{T_x^2 + T_y^2}$ (Figure 4) in the surface layer ($z = 2$ m) and in an interior layer at depth $z = 22$ m which is located in or just below the seasonal thermocline (cf. Figure 5d). Note that all of the gradient variables shown in Figure 3 and subsequent figures were calculated through the finite differences with a step of 2 m vertically and 232 m horizontally. Both the Ro and $|\Delta_H T|$ maps display a variety of submesoscale stripes of the order 10 km in length and 1 km in width. The most prominent stripes are found on the periphery of submesoscale coherent vortices (cf. Figures 3, 4 and 5), and they display a tendency to be vertically inclined towards the center of the vortex with increasing depth (see Figure 5).

Vertical/side view of the submesoscale stripes is demonstrated in Figure 5 where the Rossby number fluctuations $Ro' = Ro - \langle Ro \rangle$ and the horizontal gradient modulus of temperature and density, $|\Delta_H T|$ and $|\Delta_H \rho|$, respectively, are plotted versus distance and depth; $\langle Ro \rangle$ is the running mean value of Ro over 11 bins horizontally-neighbouring along the section (i.e. the smoothing window is 11×231.5 m $\approx$ 2.5 km). The stripes seen in the interior layers have vertical extension of 10—50 m and do not penetrate into the surface mixed layer whose thickness is only 5—8 m (cf. Figure 5b, c and d). The surface mixed layer has its own system of stripes, the vertical extension of which is probably determined by the thickness of the mixed layer but cannot be accurately estimated from Figure 5. To estimate the vertical extension of stripes in the mixed layer accurately, we calculated the correlation coefficient between the Rossby number fluctuations Ro' in the uppermost z-level (0.5 m depth) and that of 1.5, 2.5, …, 10.5 m depth. Since the correlation dropped to 0.21 for the 0.5 m and 6.5 m series and became negative (-0.013) for the 0.5 m and 7.5 m series, the vertical extension of stripes in the surface mixed layer was estimated as 6—7 m.

To diagnose the possibility of formation of submesoscale striped texture in the Baltic Sea by stirring of large-scale inhomogeneities by the eddy field, we carried out a numerical experiment with floating Lagrangian particles, similar to that described in Appendix 2. Instead of the eddy field specified by the analytical forms (A26)—(A27), we took the time-dependent (u, v)—components of currents in the surface layer of the Baltic Sea, generated by the high-resolution model. The initial concentration of floating particles was taken either homogeneous with $C_0 = 900$ particles per a 232 m $\times$ 232 m model bin, randomly seeded within the bin, or obeying a constant meridional gradient with 1000 particles per bin at the northern boundary of the study region and 800 particles per bin at the southern boundary. Keeping in mind that the typical period of rotation of coherent submesoscale vortices in the Baltic Sea is $T_{CSV} = 4\pi / f \approx$ 28 hours, we calculated the normalized concentration C/C_0 for 2018/7/18 07:07 UTC formed from the homogeneous and constant meridional gradient states during the preceding time span of $t = 8$ hours (which corresponds to the case of small advection time $t/T_{CSV} = 0.29 \ll 1$) and $t = 3$ days (which corresponds to the case of large advection time $t/T_{CSV} = 2.6 \gg 1$) (Figure 6).

In contrast to the case of non-divergent, time-dependent, 2D eddy field where the formation of striped texture by stirring of the large scale inhomogeneities took place only at $t/T_{CSV} \gg 1$ (see Appendix 2), in the case of the modelled (u, v)—components of surface currents of the Baltic Sea the striped texture in the floating particles concentration is already formed at $t/T_{CSV} \ll 1$ starting from both the homogenous and constant meridional gradient state (cf. Figures 6 and 14). Moreover, the striped texture formed from initially homogeneous and constant gradient concentration is almost identical which means that the stripes are generated by the horizontal velocity divergence/convergence rather than by stirring of the large-scale horizontal gradients by the eddy field.

The striped texture is also seen in the field of horizontal velocity divergence, but it has no simple linear relationship with the striped texture of the floating tracer (cf. Figures 6 and 7). The dissimilarity of the texture in the fields of concentration of the floating tracer and horizontal divergence is associated with a complex integral relationship between these fields (Väli et al., 2018).

$$C(\mathbf{x}, t) = C(t - \tau | \mathbf{x}, t) \exp\left[\int_{t}^{t-\tau} \operatorname{div}\big(\mathbf{u}(t' | \mathbf{x}, t)\big) dt'\right] \tag{12}$$

where $\mathbf{u} = (u, v)$ and $A(t\prime | \mathbf{x}, t)$ denotes the value of a property A at time moment $t\prime$ for a Lagrangian particle/parcel

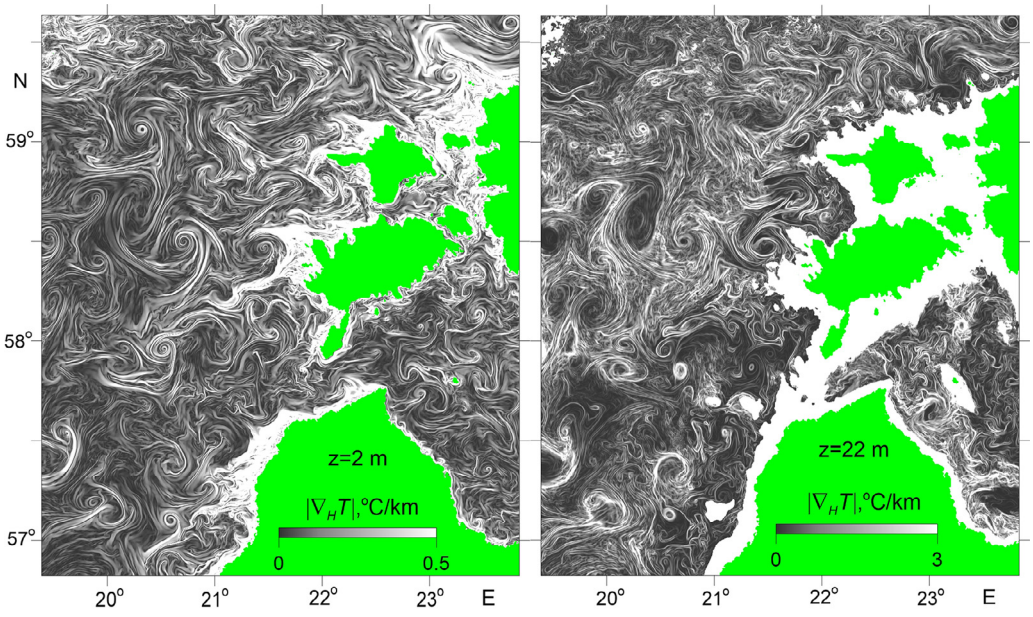

Figure 4 Horizontal temperature gradient modulus $|\nabla_H T|$ simulated on 2018/7/18 07:07 UTC at 2 m (left) and 22 m (right) levels.

that had the position $\mathbf{x} = (x, y)$ at time moment t. The quadrature solution (12) shows that concentration of floating stuff at a material point $(\mathbf{x}, t)$ is equal to the concentration at the same material point in the preceding time moment $t - \tau$ multiplied by the exponent of the backward time integral of the Lagrangian velocity divergence for the time interval $[t, t - \tau]$.

To diagnose the classic symmetric instability using the results of simulation, we tested the fulfillment of the criterion Eq. (4) and the condition $q < 0$ in the same layers as shown in Figures 2–4. A logical maps presented in Figure 8 show that the criterion Eq. (4) is satisfied in numerous elongated spots occupying approx. 20.1% of the study area in the surface layer, while at $z = 22$ m the instability percentage falls to 0.6%. Moreover, even the rare, would-be instability spots at $z = 22$ m level are not uniformly distributed within the study area but mostly located in the vicinity of the same contour of the sea depth, 22 m, i.e. they are actually in the bottom boundary layer. As to the gravitational (Eq. (2)) and inertial (Eq. (3)) instability, it is possible only in areas less than 1% of the total study area both at $z = 2$ m and $z = 22$ m (i.e. the likelihood to meet gravitational and inertial instabilities is insignificant both in the surface and interior layers).

To diagnose the McIntyre instability, we calculated parameter $Ri(1 + Ro)$ at $z = 2$ and 22 m levels (Figure 9). It was conventionally assumed that the McIntyre instability is possible at $1 \le Ri(1 + Ro) < 10$ when in accordance to Eq. (8) the Prandtl number is not too large, $1 < Pr < 40$, or not too small, $1/40 < Pr < 1$. The parameter $Ri(1 + Ro)$ was in the $1 \le Ri(1 + Ro) < 10$ range (the would-be McIntyre instability) in 39.4% and 14.0% of the study area at $z = 2$ and 22 m levels, respectively, and in the $0 < Ri(1 + Ro) < 1$ range (classic symmetric instability) in 12.6% and 0.7%, respectively. Note that the criteria Eq. (4) and Eq. (6) provide nearly the same small value for the symmetric instability percentage in the interior layer (0.6% vs 0.7%) while in the surface layer, Eq. (4) gives considerably larger value of the symmetric instability percentage relative to Eq. (6) (20.1% vs 12.6%). The discrepancy is likely caused by the vertical shear in the wind-driven Ekman currents which, being ignored in Eq. (6), can enlarge the absolute value of q_{bc} in the surface layer.

To diagnose the possibility of horizontally elongated submesoscale features to be generated by strain-induced frontogenesis, a frontogenetic strain rate was defined as $S\cos(2\theta)$, where $\theta = \theta_\rho - \theta_p$ is the angle between the density front axis θ_ρ and the principal strain axis θ_p. At $|\theta| < \pi/4$ we have $S\cos(2\theta) > 0$ which corresponds to frontogenetic situation, and at $|\theta| > \pi/4$ we have $S\cos(2\theta) < 0$ which corresponds to frontolytic situation (Hoskins, 1982, Gula et al., 2014). The horizontal strain rate S defined by Eq. (11) and the angle θ was calculated from the model output. Maps of the normalized frontogenetic strain rate $S\cos(2\theta)/f$ (Figure 10) show that positive values of this parameter of the order of 1 frequently encounter both in the surface and interior layers. The cumulative distribution function PF of the $S\cos(2\theta)/f$ parameter (Figure 11) show that the frontogenetic case is more probable than the frontolytic case ($1 - PF(0) = 0.62$ and 0.58), and the 90% quantile of PF (i.e. the value of $S\cos(2\theta)/f$ for which $PF(S\cos(2\theta)/f) = 0.9$) is 0.41 and 0.33 at $z = 2$ m and 22 m, respectively.

Distribution of the same parameters as in Figures 8–10 versus distance and depth (Figure 12) confirms that the ideal fluid SI criterion (Eq. (4)) is satisfied in numerous spots in the surface and bottom layers and not satisfied in the interior. In the surface layer, the spots do not exceed 5 m in depth. In contrast, there is some possibility for the McIntyre instability to exist both in the boundary and interior layers especially within the anticyclonic eddy (see Figure 12c). Similar to Figures 10–11, Figure 12d shows the presence of relatively high values of $S\cos(2\theta)/f$ throughout the water column.

Vertical section of the SI logical parameter, q, $Ri(1 + Ro)$, and $S\cos(2\theta)/f$ (Figure 12) confirms that conditions favourable for SI are satisfied only in a localized spots in the

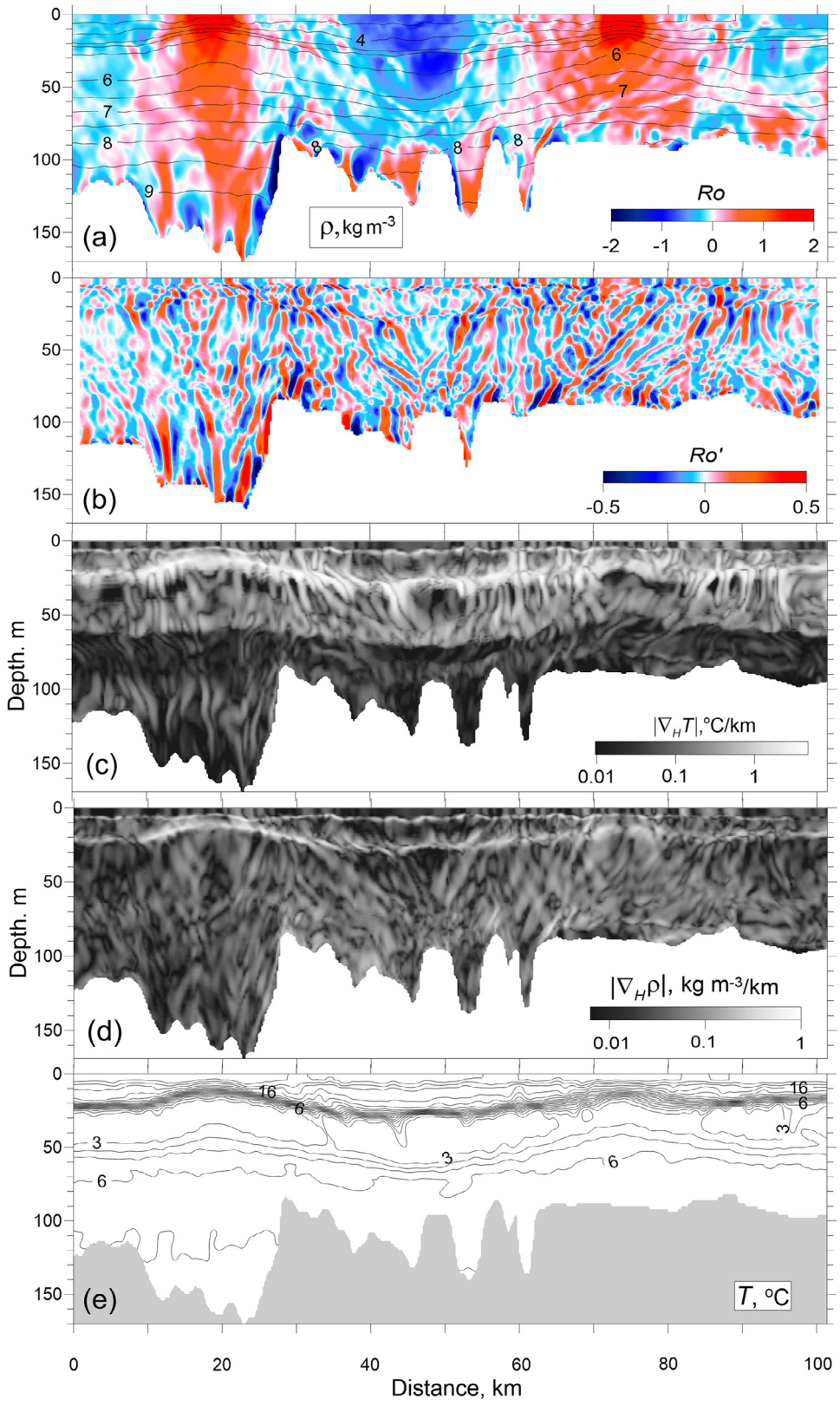

Figure 5 Vertical section through an anticyclonic and two cyclonic eddies (simulation, 2018/7/18 07:07 UTC). The position of the section is shown in Figure 3. (a) Potential density anomaly ρ (contours) and Rossby number *Ro* (colours), (b) Rossby number fluctuations *Ro*′, (c) horizontal temperature gradient modulus $|\nabla_H T|$, (d) horizontal density gradient modulus $|\nabla_H \rho|$, and (e) temperature *T* versus distance and depth.

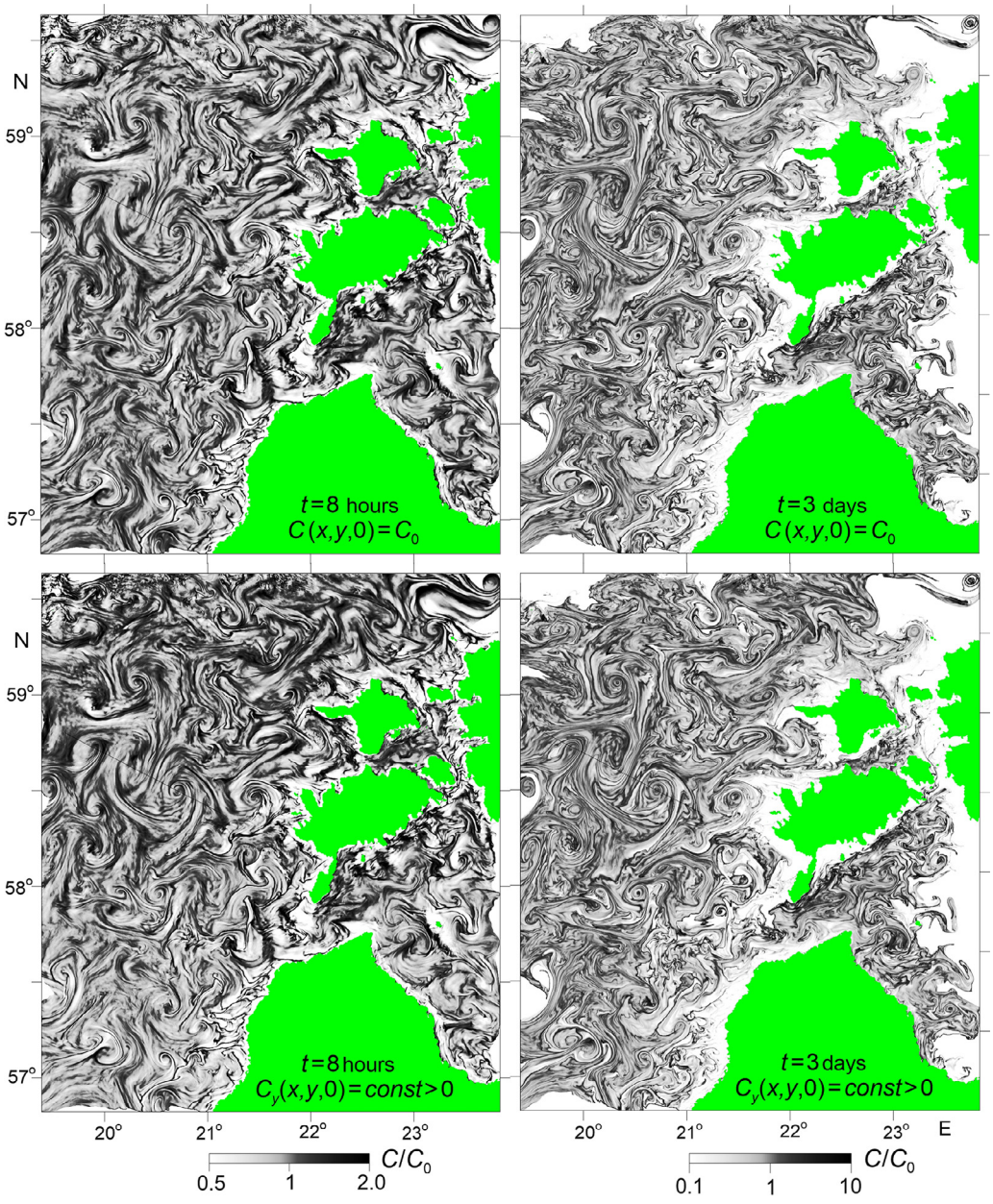

Figure 6 Normalized concentration of floating particles on 2018/7/18 07:07 UTC formed by the modelled surface layer currents during the preceding time span of $t = 8$ hours (left panels) and $t = 3$ days (right panels) from the initially homogeneous (top panels) and constant meridional gradient (bottom panels) state.

surface and bottom layers while the high positive values of the horizontal frontogenetic strain rate $S\cos(2\theta)$ of the order of f are frequently encountered everywhere throughout the water column. Note that there are some spots of negative q and $Ri(1 + Ro)$ values in the core of the anticyclonic eddy and in the bottom layer which are not confirmed by the SI logical parameter and therefore relate to the inertial instability condition $Ro < -1$.

4. Discussion and conclusions

The very high-resolution modelling of the northeastern Baltic Proper shows that preferentially along-flow elongated submesoscale inhomogeneities or stripes of the order of 10—20 km in length and 1 km in width, are quite typical for summer season both in the surface layer and the interior layers. The difference lies in the vertical scale of the stripes: it does not exceed 6—7 m in the surface layer which is comparable with the upper mixed layer depth (see Figure 5) to 10—50 m in the interior layers. In the vertical plane, the stripes display a tendency to be inclined towards the center of submesoscale coherent vortices with increasing depth. The difference in vertical size of the stripes simulated in the surface and interior layers hints at different generation mechanisms, the diagnosis of which has become the main focus of this study.

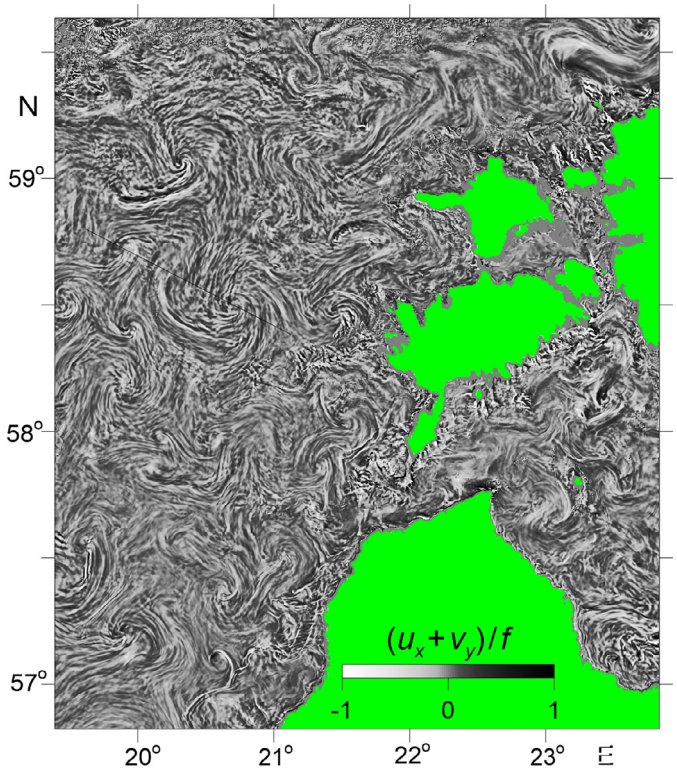

Figure 7 Normalized horizontal divergence of the surface layer velocity simulated for 2018/7/18 07:07 UTC.

Stirring of large-scale inhomogeities by the eddy field was chosen a null hypothesis for the striped texture formation. To test this, we performed a number of numerical experiments simulating horizontal advection of Lagrangian particles by the surface currents generated by the high-resolution model of the Baltic Sea and by the 2D non-divergent, time-dependent, two-gyre velocity field specified by analytical forms (A26)—(A27) for comparison. As a result, the null hypothesis was declined for the next two reasons.

First, the stirring of large-scale horizontal gradients of a passive tracer by the eddy field was found to form the striped texture for the advection time much larger than the period of eddy rotation, $t/T_{CSV} \gg 1$, while, in particular, the aggregation of floating particles in stripes by the modelled surface currents of the Baltic Sea took place already at $t/T_{CSV} \ll 1$ even when the particles were uniformly seeded throughout the study region. The latter proves that the non-uniform horizontal divergence rather than stirring of large-scale horizontal gradients matters.

Second (and more principal), stirring of large scale inhomogeneities by eddies in its narrow sense implies the possibility of striped texture formation in the passive tracer concentration (e.g. Villermaux, 2019) or in temperature and salinity provided that there are thermohaline gradients on isopycnal surfaces, i.e. thermoclinicity (Smith and Ferrari, 2009). However, the high-resolution ocean modelling forecasts the striped texture also in the dynamically active tracers such as the vertical vorticity, modulus of horizontal gradient of buoyancy, horizontal divergence, etc. Therefore, one has to seek for other mechanisms responsible for strip-like submesoscale disturbances of the velocity and buoyancy fields.

Table 1 Normalized growh rate ω_i/f of the maximum growing mode of the classic symmetric instability versus the Richardson and Rossby numbers, calculated from Eq. (A10).

Ro \\ *Ri*	0.25	0.5	0.95
-0.5	1.87	1.22	0.74
0	1.73	1	0.23
0.5	1.58	0.71	NONE

The classic SI criterion (Eq. (4)) is shown to be satisfied in numerous elongated spots occupying approximately 20% of the study area in the surface layer and the vertical extension of SI layer does not exceed 5 m and has the typical value of 4 m which is a part of the mixed layer of 6—8 m in depth (cf. Figures 5 and 12). The thermal wind velocity U in Eq. (A25) can be estimated from the model output as the product of the root mean square of the vertical velocity gradient at $z = 2$ m (which is 0.027 s^{-1} for the time moment 2018/7/18 07:07 UTC) and the height of SI layer: $U = 0.027 \times 4 \approx 0.1$ m s^{-1}. If one takes $U = 0.1$ m s^{-1}, $f = 1.24\ 10^{-4}$ s^{-1} (at 58.2°N, the mid-latitude of the study area), $Ri = 0.25$—0.5, and $Ro =$ -0.5—0.5, according to Eqs. (A10) and (A25) the SI growth timescale $T = 1/\omega_i$ will be estimated as $T = 1.2$—3.2 hours, while the upper limit for the lengthscale of growing disturbances varies within $L = 540$—3020 m (see Tables 1 and 2). These estimates of T and L seem quite reasonable, because the former is much smaller than the formation time of the submesoscale coherent vortices (McWilliams, 2016), and the latter satisfacto-

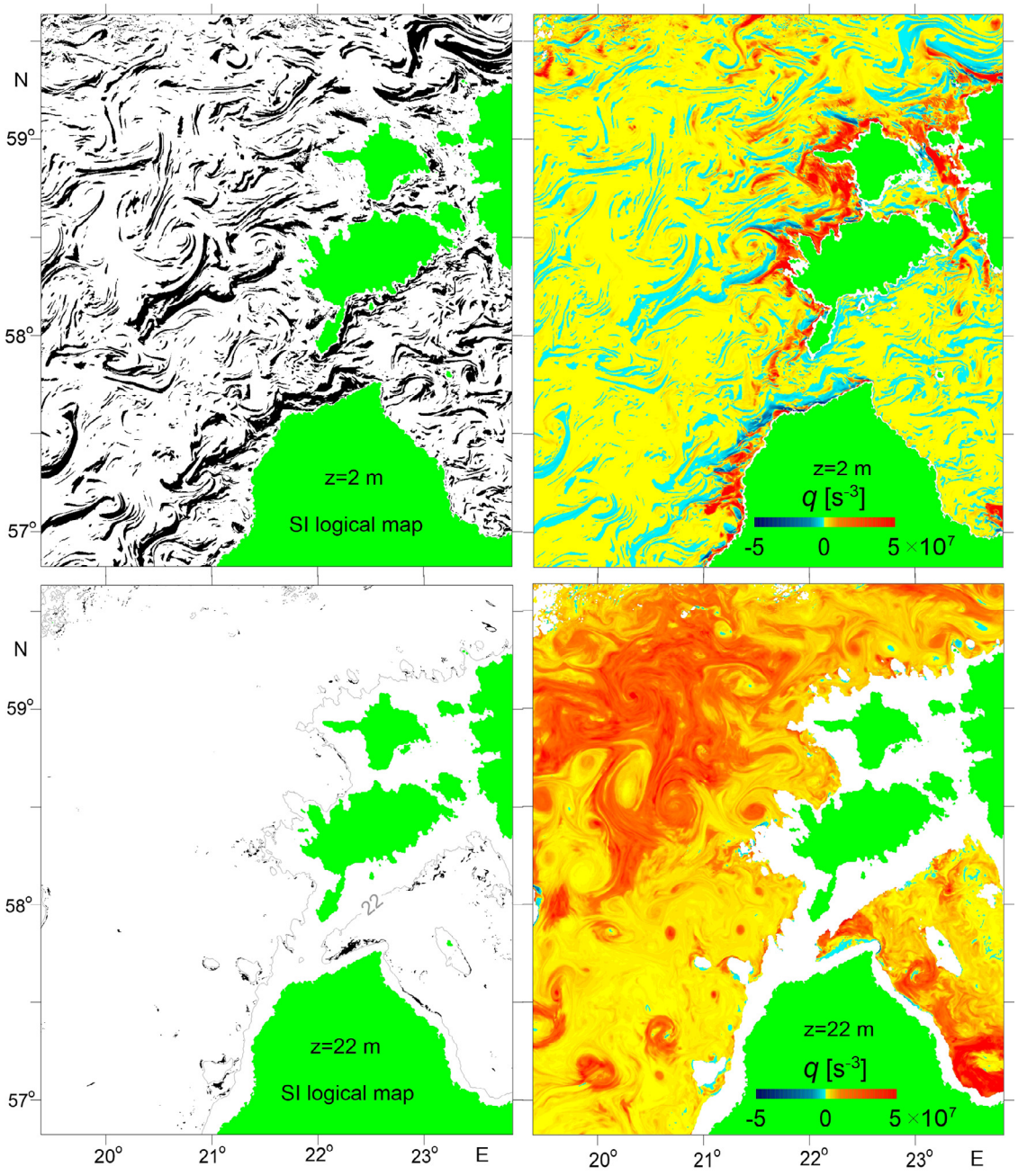

Figure 8 Logical maps (left panels) indicating where the condition for symmetric instability (Eq. (4)) is satisfied (black spots) and Ertel potential vorticity q (right panels) in the surface layer (top panels) and the interior (bottom panels) layers (simulation, 2018/7/18 07:07 UTC).

rily corresponds to the width of the simulated filaments: in accordance to Figure 5b, the horizontal wavelength of the stripes in the surface layer varies between 2 km and 3 km which is close to the upper limit of the horizontal length-scale of the unstable SI modes. Given the uncertainties both in theory and in the simulation results, a more detailed comparison of the theory with the simulation results does not seem appropriate. Therefore, symmetric instability in inviscid adiabatic fluid may be considered as a probable generation mechanism for the submesoscale stripes in the surface layer of the Baltic Sea. To the contrast, the SI criterion Eq. (4) is not satisfied in the interior layer, and alternative generation mechanisms of submesoscale stripes has to be suggested.

One of the competitive generation mechanisms of the submesoscale stripes in the interior layers of the Baltic Sea could be the McIntyre instability which is a form of symmetric instability in a viscous, non-adiabatic fluid accounting for the difference between vertical eddy viscosity and vertical eddy diffusion of buoyancy (McIntyre, 1970; Ruddick, 1992). Indeed, if we conditionally suppose that the Prandtl number Pr is as large as $Pr = 40$ or as small as $Pr = 1/40$ (so

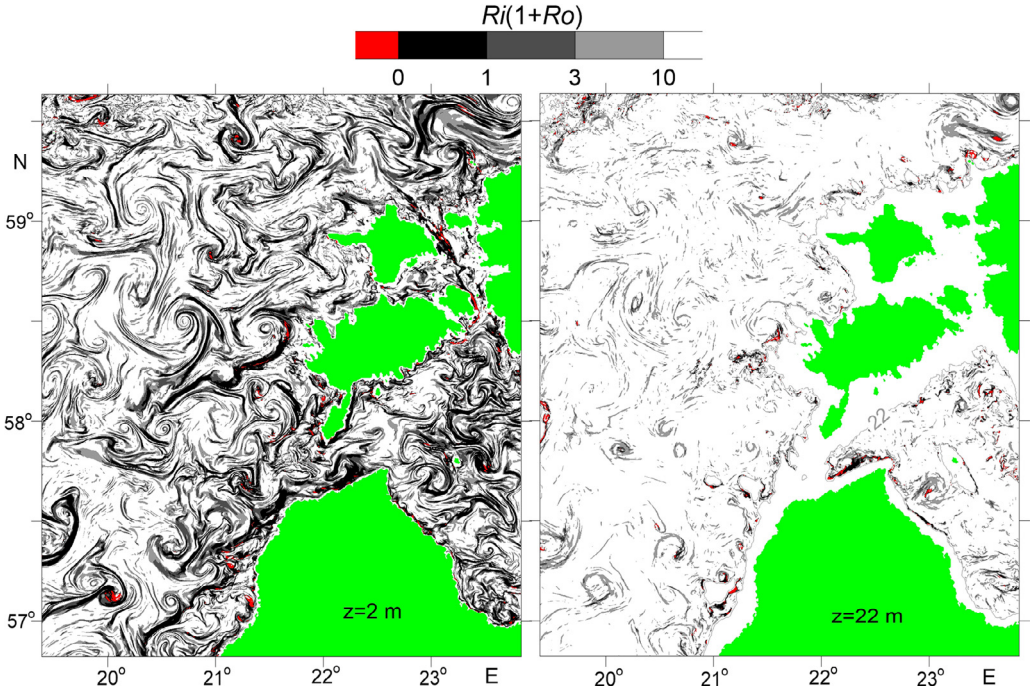

Figure 9 Parameter $Ri(1+Ro)$ in the surface and the interior layers (simulation, 2018/7/18 07:07 UTC) indicating the possibility of different instabilities: $Ri(1+Ro)<0$ — inertial instability, $0<Ri(1+Ro)<1$ — symmetric instability, $1\leq Ri(1+Ro)<(1+Pr)^2/4Pr=10$ — McIntyre instability.

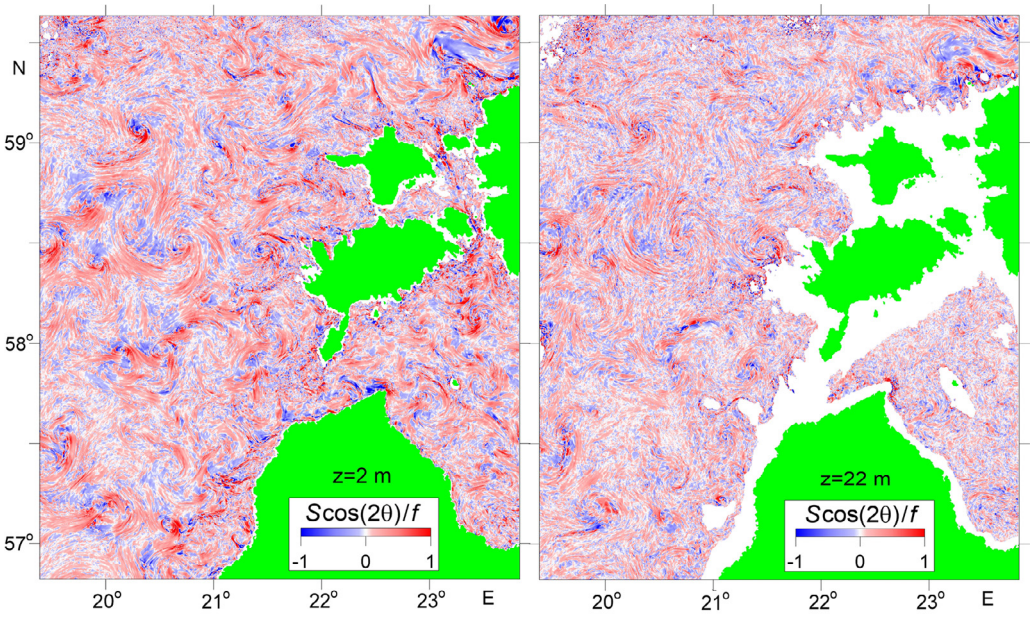

Figure 10 Normalized frontogenetic strain rate $S\cos(2\theta)/f$ in the surface (left) and interior (right) layers (simulation, 2018/7/18 07:07 UTC).

that $(1+Pr)^2/4Pr\approx 10$), the McIntyre instability criterion $1<Ri(1+Ro)<(1+Pr)^2/(4Pr)$ will be satisfied in approx. 39% of the study area in the surface layer, while in the interior layers, the percentage falls to 14% (see Figures 9 and 12c). The latter percentage value, 14%, being considerably smaller than in the surface layer, is still large enough to consider the McIntyre instability as a competitive generation mechanism for submesoscale stripes in the interior layers. As to the growth time of the McIntyre instability, it is considerably larger than respective estimates for the clas-

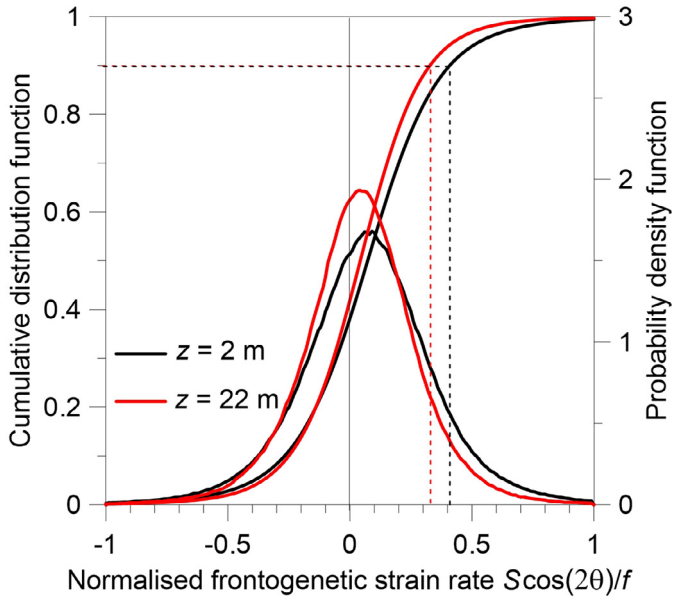

Figure 11 Cumulative distribution functions and probability density functions of the normalized frontogenetic strain rate $S\cos(2\theta)/f$ in the surface layer (black curves) and the interior (red curves) calculated from the model output on 2018/7/18 07:07 UTC. Dotted lines point at 90% quantile of the $S\cos(2\theta)/f$ distributions.

Table 2 Limitation for the horizontal length scale of disturbances L growing due to the classic symmetric instability, calculated from Eq. (A25) at $U = 0.1$ m s^{-1}, $f = 1.24\bullet10^{-4}$ s^{-1}, and different values of the Richardson and Rossby numbers.

Ro \\ *Ri*	0.25	0.5	0.95
-0.5	<3020 m	<2800 m	<2340 m
0	<1400 m	<1140 m	<360 m
0.5	<860 m	<540 m	NONE

Table 3 Normalized growth rate ω_i/f of the maximum growing mode of the McIntyre instability versus the Richardson, Rossby, and Prandtl numbers (*Ri*, *Ro*, and *Pr*, respectively), calculated as the maximum positive root of the polynomial (A15). The choice of *Pr* values, 6, 1/6, 10, 1/10, 40 and 1/40, is motivated by the desire to have approx. 2, 3, and 10 for the respective values of $(1+\mathrm{Pr})^2/4Pr$ (see Eq. (8) and Figures 9 and 12c). Note that the case of $Ri = 1$, $Ro = -0.5$ does not correspond to the McIntyre instability because $Ri(1+Ro) = 0.5 < 1$.

Ro = 0			
Pr \\ *Ri*	1.1	2	5
6 (1/6)	0.096 (0.28)	0.00032 (0.0017)	<0
10 (1/10)	0.12 (0.45)	0.018 (0.13)	<0
40 (1/40)	0.15 (1.1)	0.055 (0.69)	0.0095 (0.23)
Ro = 0.5			
Pr \\ *Ri*	1.1	2.2	5
6 (1/6)	-	0.066 (0.20)	<0
10 (1/10)	-	0.084 (0.32)	0.0035 (0.029)
40 (1/40)	-	0.11 (0.77)	0.027 (0.40)

sic SI (cf. Tables 1 and 3). There is some doubt that the McIntyre instability at $Pr > 1$ (viscous destabilization) can be responsible for generation of submesoscale stripes simulated in the interior layer of the Baltic Sea for two reasons. First, the typical value of the growth time $1/\omega_i$, achieved when $Ri(1+Ro)$ is in the middle of the instability range $(1,\ (1+Pr)^2/4Pr > 1)$, is estimated at 3 days (see Table 3) which is comparable with the formation time of the submesoscale coherent vortices. Second, the slope of simulated stripes clearly exceeds the isopycnal slope (see Figure 5), while the theory forecasts the opposite (see Eq. (A18)).

Despite the fact that now we have no physical reason to believe that the Prandtl number in the ocean can be less than one, it still seems interesting to consider the McIntyre instability under the condition $Pr < 1$ (diffusive destabilization). In this case, in accordance to Eq. (A18), the slope of growing disturbances is larger than the isopycnal slope which is consistent with the slopes of stripes simulated in the interior layers (see Figure 5b and c). Moreover, the growth rates of the maximum growing disturbances calculated from Eq. (A15) at $Pr < 1$ are found to be much larger than that of $Pr > 1$ (see Table 3). For example, at $Ro = 1$, $Ri = 2$, $Pr = 14$ we have $\omega_i/f = 0.031$ (the growth time is $1/\omega_i \approx 3$ days) versus $\omega_i/f = 0.24$ (the growth time is $1/\omega_i \approx 9$ hours) at $Ro = 1$, $Ri = 2$, $Pr = 1/14$.

The credibility of generation of submesoscale stripes by strain-induced frontogenesis, can be evaluated by considering the 90% quantile of the probability function of the normalized frontogenetic strain rate $PF(S\cos(2\theta)/f)$. The high-resolution modelling show that the condition $PF(S\cos(2\theta)/f) = 0.9$ is satisfied at $[S\cos(2\theta)/f]_{0.9} = 0.41$ and 0.33 at $z = 2$ m and 22 m, respectively. In this case,

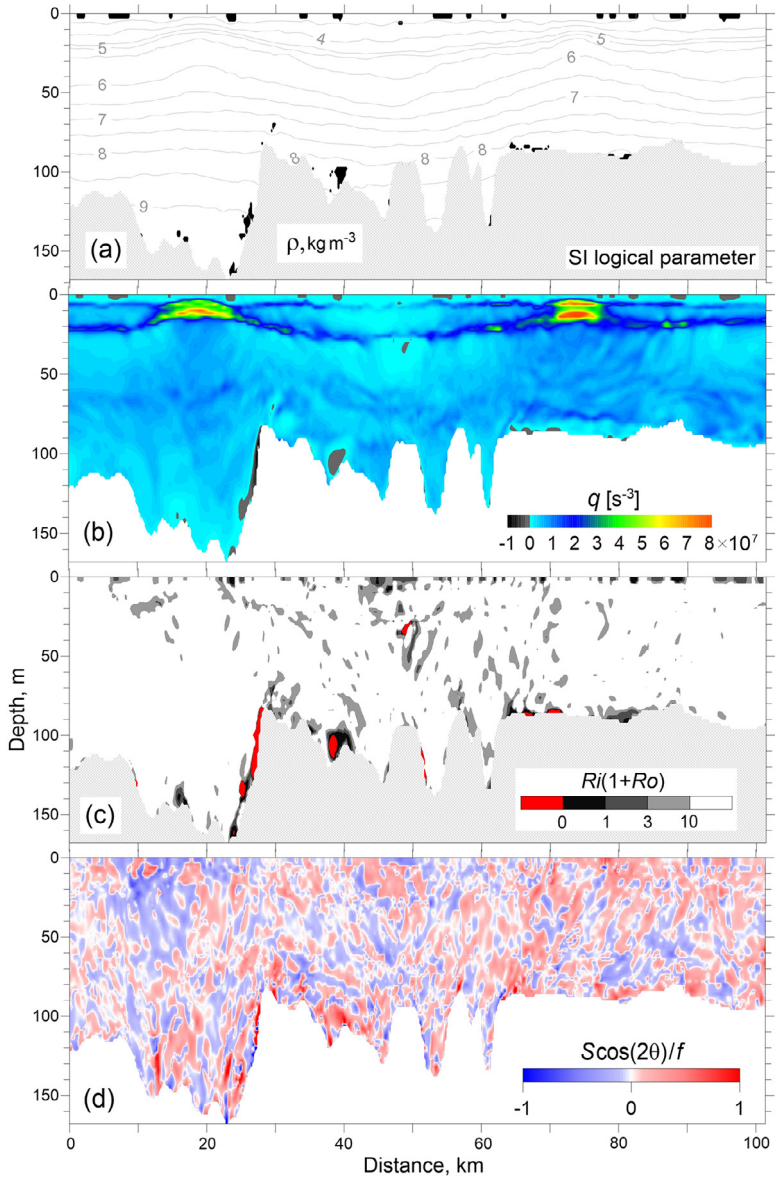

Figure 12 Vertical section through an anticyclonic and two cyclonic eddies (simulation, 2018/7/18 07:07 UTC). The position of the section is shown in Figures 2 and 3. (a) Potential density anomaly σ_θ (contours) and SI logical parameter based on Eq. (4) criterion (black spots), (b) Ertel potential vorticity q calculated using Eq. (1), (c) instability parameter $Ri(1+Ro)$, and (d) normalized frontogenetic rate $S\cos(2\theta)/f$ versus distance and depth.

a characteristic growth time of submesoscale stripes due to frontogenesis can be estimated as $1/(0.41f) = 5.5$ hours and $1/(0.33f) = 6.8$ hours in the surface and interior layers, respectively, which is 2—4 times longer than the above mentioned SI growth times in the mixed layer.

Summarizing the above consideration, we admit that three of four processes considered (the classic symmetric instability, the McIntyre instability, and the strain-induced frontogenesis) could contribute to generation of the submesoscale striped texture in the surface layer of the Baltic Sea, while in the interior layers, the classic symmetric instability is excluded. Taking into account the fact that out of several competing processes, the fastest survives, we conclude that the classic symmetric instability and the strain-induced frontogenesis are the most probable mechanisms responsible for the formation of submesoscale striped texture in the surface mixed layer of the Baltic Sea. In the interior layers, the strain-induced frontogenesis and hypothetically the McIntyre instability can be essential, but it takes further effort to draw a more definite conclusions. Stirring of large-scale inhomogeneities by the eddy field could be responsible for formation of striped texture in a passive tracer concentration and in temperature and salinity in the presence of thermoclinicity, but it does not imply formation of stripes in dynamically active tracers, such as vertical vorticity, horizontal gradients of buoyancy, etc. The DDSI is excluded from a list of possible mechanisms of formation of submesoscale stripes because the study area in the period considered was almost free of thermoclinicity, and double diffusion was therefore unable to generate alternating hor-

izontal pressure gradients. Note that the presence of submesoscale striped structures in the surface layer is backed up by remote sensing images, while the simulated deeper-layer filaments do not yet have such a strong observational support.

All the above-described processing and analysis of the model output was performed for one point in the simulation time — 2018/07/18, and therefore the question arises as to how typical the obtained results are. The same processing of the model output was carried out for two more points in time — 2018/07/27 and 2018/08/03 for which we have the remote sensing images similar to Figure 2, a and b (not shown in the article). Since no significant differences were found, the above results can be considered apparently typical for the summer season in the Baltic Sea.

Declaration of competing interest

The authors declare that they have no known competing financial interests or personal relationships that could have appeared to influence the work reported in this paper.

Acknowledgements

The allocation of computing time on High Performance Computing cluster by the Tallinn University of Technology and by the University of Tartu is gratefully acknowledged. The GETM community in Leibniz Institute of Baltic Sea Research (IOW) is acknowledged for their technical support and the maintenance of model code. Dmitry Solov'ev from Marine Hydrophysical Institute, Sevastopol, is acknowledged for presenting the remote sensing images. Germo Väli (submesoscale circulation modelling, discussing the results) was supported by the Estonian Research Council (grant no. PRG602 and grant no. IUT19-6). Victor Zhurbas (processing and interpreting the simulation data, preparation of the manuscript) and Natalia Kuzmina (instability analysis, discussing the results) were supported by budgetary financing of the Shirshov Institute of Oceanology RAS (Project No. 0128-2021-0001).

Appendix 1. Instability analysis

Let us perform a simple analysis of the instability of a geostrophic flow with a linear vertical velocity profile in the framework of a 2D problem, that is, when the perturbations do not depend on the along-flow coordinate x (symmetric instability). The basic flow equations are

$$fU = -\frac{\partial \bar{P}}{\partial y};\ V = 0;\ W = 0,\ \frac{\partial \bar{P}}{\partial z} = -g\bar{\rho}$$

where $\bar{P}$ and $\bar{\rho}$ are the pressure and density divided by the reference density ρ_0; the vertical shear of the basic flow is taken constant: $\frac{\partial U}{\partial z} = \frac{g}{f}\frac{\partial \bar{\rho}}{\partial y} = const$. We take into account also a constant barotropic shear of the basic flow: $\frac{\partial U}{\partial y} = const$.

Equations for disturbances with allowance for viscosity and diffusion of buoyancy are

$$\frac{\partial u}{\partial t} - fv + v\frac{\partial U}{\partial y} + w\frac{\partial U}{\partial z} = Pr \cdot K\frac{\partial^2 u}{\partial z^2} \tag{A1}$$

$$\frac{\partial v}{\partial t} + fu = -\frac{\partial p}{\partial y} + Pr \cdot K\frac{\partial^2 v}{\partial z^2} \tag{A2}$$

$$\frac{\partial w}{\partial t} + g\rho = -\frac{\partial p}{\partial z} \tag{A3}$$

$$\frac{\partial v}{\partial y} + \frac{\partial w}{\partial z} = 0 \tag{A4}$$

$$\frac{\partial \rho}{\partial t} + v\frac{\partial \bar{\rho}}{\partial y} + w\frac{\partial \bar{\rho}}{\partial z} = K\frac{\partial^2 \rho}{\partial z^2} \tag{A5}$$

where u, v, and w are components of velocity disturbances, p and ρ are disturbances of pressure and density divided by ρ_0, and K is the vertical diffusion of buoyancy.

In the case of infinite depth layer, the solution of system Eq. (A1)—(A5) is sought in the form

$$\psi = \psi_0 \exp(\omega t + imz + ily) \tag{A6}$$

where ψ is any disturbed variable from Eq. (A1)—(A5). Note that with this form of solution, the tangent of the angle of inclination of the disturbances relative to the horizontal (slope) is

$$\tan(\gamma) = -\frac{l}{m}$$

Let's consider different cases of the Eq. (A1)—(A6) solutions.

A1. Inviscid adiabatic fluid in hydrostatic approximation, infinite depth layer

After removing the last term in the right hand part of Eq. (A1), (A2), and (A5) and substituting Eq. (A6) to Eq. (A1)—(A5) the following equation for the growth rate ω is obtained

$$\omega^2 + ff^* + 2\tan(\gamma_\rho)N^2\frac{l}{m} + N^2\frac{l^2}{m^2} = 0 \tag{A7}$$

where $\tan(\gamma_\rho) = \frac{g\bar{\rho}_y}{N^2}$ is the slope of isopycnals relative to the horizontal, $f^* = f - \frac{\partial U}{\partial y}$. For a small isopycnal slope, $\gamma_\rho \ll 1$, $\tan(\gamma_\rho) \approx \gamma_\rho$, and Eq. (A7) re-writes as

$$\omega^2 + ff^* + N^2(l/m + \gamma_\rho)^2 - N^2\gamma_\rho^2 = 0 \tag{A7a}$$

It follows from Eq. (A7a)′ that instability (i.e., $\omega > 0$) is possible only when $\gamma_\rho^2 - \frac{ff^*}{N^2} > 0$ or

$$Ri(1 + Ro) < 1 \tag{A8}$$

where $Ri = \frac{f^2}{N^2\gamma_\rho^2}$ is the geostrophic Richardson number and $Ro = -\frac{\partial U/\partial y}{f}$ is the gradient Rossby number. Note that Eq. (A8) fits the classic SI instability condition Eq. (6). Based on the results of Ooyama (1966) Eq. (A8) was probably first obtained by Hoskins (1974).

According to Eq. (A7a)′, the slope of the maximum growing disturbances, γ_i, is

$$\gamma_i = -\left(\frac{l}{m}\right)_i = \gamma_\rho \tag{A9}$$

i.e., the maximum growing disturbance does not cross the isopycnal surfaces (see also Kuznima and Zhurbas, 2000; McIntyre, 1970; Taylor and Ferrari, 2009). The growth rate of the maximum growing disturbances, ω_i, is

$$\omega_i = f\left(\frac{1 - Ri(1+Ro)}{Ri}\right)^{1/2} \tag{A10}$$

Note that Eq. (A10) coincides the well-known formula by Stone (1966), provided that $Ro = 0$ (cf. Eq. (7) which was derived in Stone (1966) for the no barotropic shear case). Eq. (A10) was also derived in Haine and Marshall (1998) from energy analysis of the thermal wind.

A2. Inviscid adiabatic fluid, non-hydrostatic case, infinite depth layer

In this case, the equation for the growth rate is

$$\omega^2\left(1 + \frac{l^2}{m^2}\right) + ff^* + 2\tan(\gamma_\rho)N^2\frac{l}{m} + N^2\frac{l^2}{m^2} = 0 \tag{A11}$$

It can be easily shown by analogy with the previous analysis, that the instability condition and the slope of the maximum growing mode remain the same as in the hydrostatic case (see Eq. (A8) and (A9)). However, the growth rate for the maximum growing disturbances is expressed in this case by the formula:

$$\omega_i = \left(\frac{(\tan(\gamma_\rho))^2N^2}{1 + (\tan(\gamma_\rho))^2} - \frac{ff^*}{1 + (\tan(\gamma_\rho))^2}\right)^{1/2} \tag{A12}$$

For small isopycnal slopes $\tan(\gamma_\rho) \ll 1$ Eq. (A12) reduces to Eq. (A10), while for large isopycnal slopes $\tan(\gamma_\rho) \gg 1$ it reduces to

$$\omega_i = N\sqrt{1 - Ri(1+Ro)} \tag{A13}$$

Thus, the maximum growing perturbations can grow practically in a few minutes, but only when the slope of the isopycnal surfaces significantly exceeds the angle of $\pi/4$.

A3. Viscous non-adiabatic fluid in hydrostatic approximation, infinite depth layer

In this case we take $\tan(\gamma_\rho) \approx \gamma_\rho \ll 1$, and the growth rate equation is

$$\frac{A \cdot B}{N^2} + \frac{l}{m}\gamma_\rho\left(1 + \frac{B}{A}\right) + \frac{ff^*}{N^2}\frac{B}{A} + \frac{l^2}{m^2} = 0 \tag{A14}$$

where $A = \omega + PrKm^2$, and $B = \omega + Km^2$. If $Pr \neq 1$, Eq. (A14) is reduced to a polynomial of the third degree:

$$\omega^3 + C_2\omega^2 + C_1\omega + C_0 = 0 \tag{A15}$$

It can be easily shown that the coefficients C_1 and C_2 in Eq. (A15) are nonnegative when $Ri(1+Ro) \geq 1$. Therefore, for $Ri(1+Ro) \geq 1$ the polynomial Eq. (A15) has one and only one positive real root and only when $C_0 < 0$. To analyze the dissipation-related instability, let's consider the free term of Eq. (A15),

$$C_0 = Km^2\left(Pr^2K^2m^4 + \gamma_\rho\frac{l}{m}(Pr+1)N^2 \quad + ff^* + PrN^2\frac{l^2}{m^2}\right) \tag{A16}$$

which can be re-written as

$$C_0 = Km^2N^2Pr\left(\frac{PrK^2m^4}{N^2} + \frac{ff^*}{PrN^2} + \left(\frac{\gamma_\rho(Pr+1)}{2Pr} + \frac{l}{m}\right)^2 - \frac{\gamma_\rho^2(Pr+1)^2}{4Pr^2}\right) \tag{A16a}$$

It follows from Eq. (A16a)′ that the free term C_0 can be negative only if

$$\frac{ff^*}{\gamma_\rho^2N^2} = Ri(1+Ro) < \frac{(Pr+1)^2}{4Pr} \tag{A17}$$

which is a well-known condition for the McIntyre (1970) instability at $Pr \neq 1$ (cf. Eq. (A17) and Eq. (8)). When the conditions $1 \leq Ri(1+Ro) < \frac{(Pr+1)^2}{4Pr}$ and $Pr \neq 1$ are satisfied the slope of the maximum growing mode in accordance to (A16a)′ is

$$\gamma_i = -\left(\frac{l}{m}\right)_i = \gamma_\rho\frac{Pr+1}{2Pr} \tag{A18}$$

Equation (A18) says that for the McIntyre instability the slope of the maximum growing mode exceeds the isopycnal slope when $Pr < 1$ and becomes less than it when $Pr > 1$. Note that at $Pr = 1$ the instability criterion remains the same as in the case of ideal fluid (McIntyre, 1970).

A4. Inviscid adiabatic fluid in hydrostatic approximation, finite depth layer

In contrast to the slope and growth rate of the maximum growing mode (Eq. (A9) and (A10)), the characteristic length scale of instability cannot be found from the inviscid adiabatic consideration in the infinite depth layer. To estimate the characteristic length scale of instability, let's consider, following Stone (1966), a finite depth layer with the barotropic shear additionally included and seek the solution of system of equations (A1)–(A5) with hydrostatic approximation in the form

$$\psi = \psi_0(z)\exp(\omega t + ily) \tag{A19}$$

Substitution of Eq. (A19) into Eq. (A1)–(A5) reduces the latter to a second-order differential equation relative to the vertical velocity w with constant coefficients, which should be solved under the boundary conditions

$$w = 0 \text{ at } z = 0,\ H \tag{A20}$$

where H is the layer depth. Here, for the sake of brevity, we present only the equation for the growth rate, which is the result of solving the eigenvalue problem:

$$\left(\frac{\gamma_\rho lN^2}{\omega^2 + ff^*}\right)^2 = \frac{l^2N^2}{\omega^2 + ff^*} + \frac{\pi^2n^2}{H^2},\ (n = 1, 2, 3\ldots) \tag{A21}$$

The maximally growing mode is realized at $n = 1$.

It is easy to see from Eq. (A21) that, with the infinitely deep layer (that is, when the last term on the right-hand side of Eq. (A21) tends to zero), the formula for the growth rate fully corresponds to Eq. (A10). For a layer of finite depth, Eq. (A21) is reduced to a fourth-degree polynomial

$$\omega^4 + C_2\omega^2 + C_0 = 0 \tag{A22}$$

Keeping in mind that in Eq. (A22) $C_2 > 0$ if $Ro > -1$, the symmetric instability is possible only when $C_0 < 0$, i.e. when

$$l^2N^2 f f^* - \gamma_\rho^2 l^2 N^4 + \frac{\pi^2 (f f^*)^2}{H^2} < 0 \tag{A23}$$

It follows from Eq. (A23) that instability is possible when Eq. (A8) is satisfied, and the unstable wavenumber l lies in the range

$$l^2 > \frac{(\pi f(1+Ro))^2}{U^2(1-Ri(1+Ro))} \tag{A24}$$

where U is the maximum velocity of the basic geostrophic flow. The horizontal length scale of unstable disturbances should therefore satisfy the inequality

$$L = \frac{2\pi}{l} < \frac{2U(1-Ri(1+Ro))^{1/2}}{f(1+Ro)} \tag{A25}$$

Formula (A24) without barotropic shear included (at $Ro = 0$) was first obtained by Stone (Stone, 1966). Note that in the considered problem it is impossible to find the growth rate of the maximum growing perturbation: the larger the wavenumber l, the greater the growth rate. This is a disadvantage of this problem, which should be further fixed by taking friction into account. However, one can assume that it would not result in a large error in some cases of observations in the ocean to estimate the maximum growth rate of disturbances in a layer of finite depth using Stone's (1966) formula Eq. (A10). Relation Eq. (A21) helps to choose such cases. If the ratio $\frac{lN}{f} \gg \frac{\pi}{H}$ is satisfied, then the estimate of the growth rate using formula Eq. (A10) is satisfactory.

Appendix 2. Formation of striped texture by stirring of large scale inhomogeneities by the eddy field: an illustrating example

Let's consider an illustrating example of the formation of striped texture by stirring of large scale gradients in a 2D, periodically varying double-gyre velocity field described by the stream-function (Shadden et al., 2005)

$$\psi(x, y, t) = A \sin(\pi f(x, t)) \sin(\pi y) \tag{A26}$$

where

$$f(x, t) = a(t)x^2 + b(t)x,\ a(t) = \varepsilon \sin(\omega t),\ b(t) = 1 - 2\varepsilon \sin(\omega t) \tag{A27}$$

over the domain $[0, 2] \times [0, 1]$. The analytical forms (A26)–(A27) are chosen to produce a simple, time-dependent two-gyre flow with fixed boundaries, not to approach a solution of Navier–Stokes' equations. For $\varepsilon \neq 0$ the flow consists of two gyres that conversely expand and contract periodically in the x-direction such that the rectangle enclosing the gyres remains invariant. The velocity field $u = -\psi_y$, $v = \psi_x$ and vorticity $\zeta = -u_y + v_x$ generated

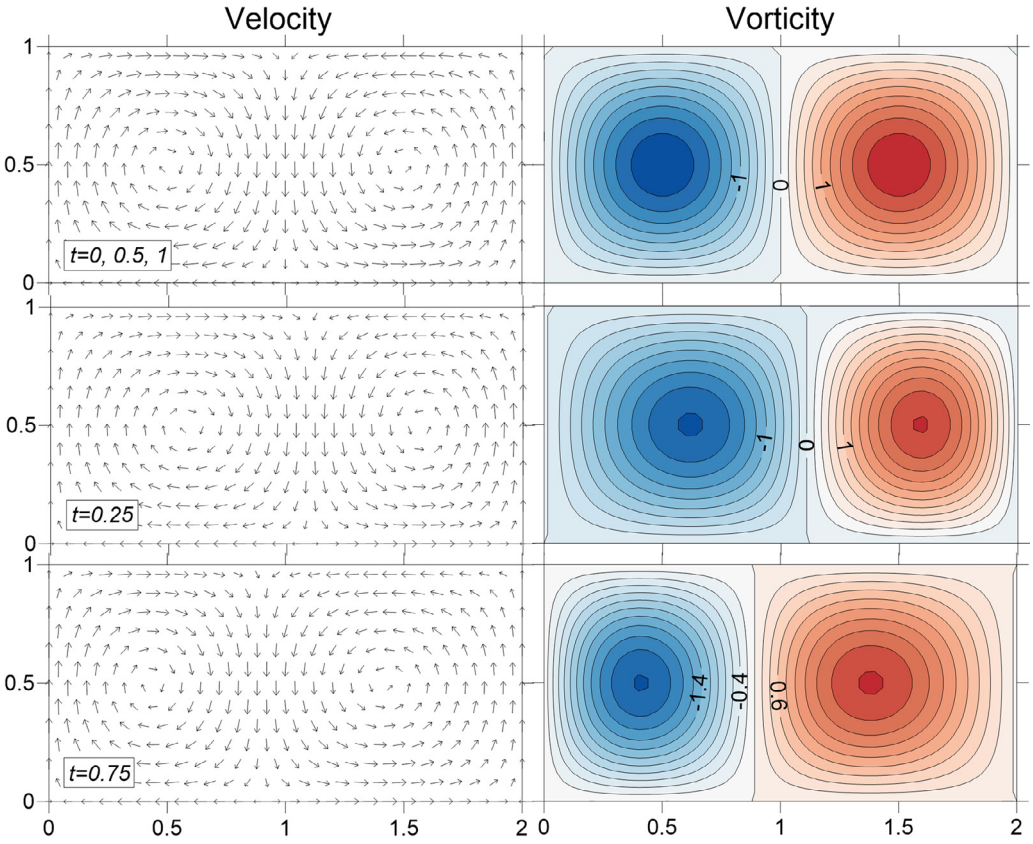

Figure 13 Velocity and vorticity fields generated by the analytical forms Eqs. (A26)–(A27) for $A = 0.1$, $\varepsilon = 0.1$, $\omega = 2\pi$ at the time moments $t = 0,\ 0.25,\ 0.5,\ 0.75,\ 1$.

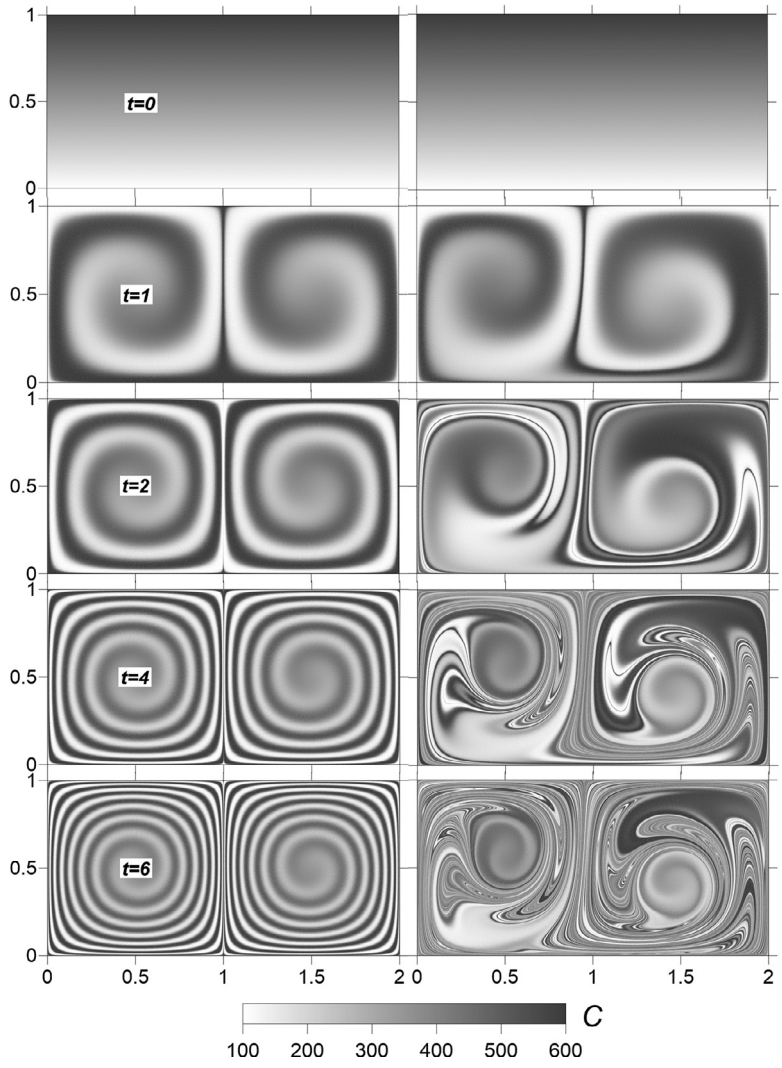

Figure 14 Evolution of a constant y-gradient of tracer concentration in the two-gyre velocity field shown in Figure 13. The left panels correspond to the stationary case ($\varepsilon = 0$), and the right panels to the non-stationary case at $\varepsilon = 0.1$.

by the analytical forms (A26)—(A27) for $A = 0.1$, $\varepsilon = 0.1$, $\omega = 2\pi$ at different time moments are shown in Figure 13.

Advection of a passive tracer is described by the balance equation

$$C_t + (uC)_x + (vC)_y = \frac{dC}{dt} + C\,\mathrm{div}(\mathbf{u}) = 0 \qquad \text{(A28)}$$

where $C(x, y, t)$ is the tracer concentration, $\frac{dC}{dt} = C_t + uC_x + vC_y$ is the time derivative of concentration in the Lagrangian frame, and $\mathrm{div}(\mathbf{u}) = u_x + v_y$ is the velocity divergence. Let's set the initial condition as a constant y-gradient of concentration

$$C(x, y, 0) = 100 + 500y, \quad x = [0,\ 2],\ y = [0,\ 1] \qquad \text{(A29)}$$

and integrate Eq. (A28) numerically with the velocity field (A26)—(A27) for $A = 0.1$, $\omega = 2\pi$, and $\varepsilon = 0$ (stationary case) and $\varepsilon = 0.1$ (non-stationary case), using a Lagrangian trajectories approach as described in Väli et al. (2018). The numerical solution presented in Figure 14 shows that in the stationary velocity field at $t \gg 1$, where $t = 1$ corresponds to the period of eddy rotation, the initial constant gradient of concentration is wound in a spiral-like stripe of enhanced concentration, and the number of cycles in the stripe increases as t. In the non-stationary case, where $t = 1$ corresponds to both the eddy rotation and eddy expansion-contraction periods, a complicated striped texture is formed at $t \gg 1$. The number of stripes per eddy is likely determined by superposition of two periodical processes and drastically increases with t.

References

Bachman, S.D., Fox-Kemper, B., Taylor, J.R., Thomas, L.N., 2017. Parameterization of frontal symmetric instabilities. I: Theory for resolved fronts. Ocean Model. 109, 72—95. https://doi.org/10.1016/j.ocemod.2016.12.003

Barkan, R., Molemaker, M.J., Srinivasan, K., McWilliams, J.C., D'Asaro, E.A., 2019. The role of horizontal divergence in submesoscale frontogenesis. J. Phys. Oceanogr. 49, 1593—1618. https://doi.org/10.1175/JPO-D-18-0162.1

Brannigan, L., Marshall, D.P., Garabato, A.C.N., Nurser, A.J.G., 2017. Submesoscale instabilities in mesoscale eddies. J. Phys. Oceanogr. 47, 3061—3085. https://doi.org/10.1175/JPO-D-16-0178.1

Burchard, H., Bolding, K., 2001. Comparative Analysis of Four Second-Moment Turbulence Closure Models for the Oceanic Mixed Layer. J. Phys. Oceanogr. 31, 1943—1968. https://doi.org/10.1175/1520-0485(2001)031⟨1943:CAOFSM⟩2.0.CO;2

Burchard, H., Bolding, K., 2002. GETM — a general estuarine transport model. Scientific documentation, Technical report EUR 20253 en. In: Tech. rep., European Commission. Ispra, Italy.

Canuto, V.M., Howard, A., Cheng, Y., Dubovikov, M.S., 2001. Ocean Turbulence. Part I: One-Point Closure Model—Momentum and Heat Vertical Diffusivities. J. Phys. Oceanogr. 31, 1413—1426. https://doi.org/10.1175/1520-0485(2001)031⟨1413:OTPIOP⟩2.0.CO;2

Capet, X., McWilliams, J.C., Molemaker, M.J., Shchepetkin, A.F., 2008. Mesoscale to Submesoscale Transition in the California Current System. Part II: Frontal Processes. J. Phys. Oceanogr. 38 (1), 44—64. https://doi.org/10.1175/2007JPO3672.1

Choi, J., Bracco, A., Barkan, R., Shchepetkin, A.F., McWilliams, J.C., Molemaker, J.M., 2017. Submesoscale dynamics in the Northern Gulf of Mexico. Part III: Lagrangian implications. J. Phys. Oceanogr. 47, 2361—2376. https://doi.org/10.1175/JPO-D-17-0036.1

Chrysagi, E., Umlauf, L., Holterrmann, P., Klingbeil, K., 2021. High-resolution simulations of submesocale processes in the Baltic Sea. J. Geophys. Res. Oceans 126, e2020JC016411. https://doi.org/10.1029/2020JC016411

D'Asaro, E.A., Shcherbina, A.Y., Klymak, J.M., Molemaker, J., Novelli, G., Guigand, C.M., Haza, A.C., Haus, B.K., Ryan, E.H., Jacobs, G.A., Huntley, H.S., Laxague, N.J.M., Chen, S., Judt, F., McWilliams, J.C., Barkan, R., Kirwan Jr., A.D., Poje, A.C., Özgökmen, T.M., 2018. Ocean convergence and the dispersion of flotsam. Proc. Nat'l Acad. Sci. USA 115, 1162—1167. https://doi.org/10.1073/pnas.1802701115

Finni, T., Kononen, K., Olsonen, R., Wallström, K., 2001. The history of cyanobacteria blooms in the Baltic Sea. Ambio 30 (4—5), 172—178.

Flather, R.A., 1994. A storm surge prediction model for the northern Bay of Bengal with application to the cyclone disaster in April 1991. J. Phys. Oceanogr. 24, 172—190. https://doi.org/10.1175/1520-0485(1994)024⟨0172:ASSPMF⟩2.0.CO;2

Garrett, C., MacCready, P., Rhines, P., 1993. Arrested Ekman layers: Rotating stratified flow near a sloping boundary. Annu. Rev. Fluid Mech. 25, 291—323.

Giudici, A., Suara, K.A., Soomere, T., Brown, R., 2021. Tracking areas with increased likelihood of surface particle aggregation in the Gulf of Finland: A first look at persistent Lagrangian Coherent Structures (LCS). J. Mar. Syst. 217, 103514. https://doi.org/10.1016/j.jmarsys.2021.103514

Gräwe, U., Holtermann, P., Klingbeil, K., Burchard, H., 2015. Advantages of vertically adaptive coordinates in numerical models of stratified shelf seas. Ocean Model. 92, 56—68.

Gula, J., Molemaker, M.J., McWilliams, J.C., 2014. Submesoscale cold filaments in the Gulf Stream. J. Phys. Oceanogr. 44, 2617—2643. https://doi.org/10.1175/JPO-D-14-0029.1

Gula, J., Molemaker, M.J., McWilliams, J.C., 2016. Submesoscale dynamics of a Gulf Stream frontal eddy in the South Atlantic Bight. J. Phys. Oceanogr. 46, 305—325. https://doi.org/10.1175/JPO-D-14-0258.1

Haine, T.W., Marshall, J., 1998. Gravitational, symmetric, and baroclinic instability of the ocean mixed layer. J. Phys. Oceanogr. 28 (4), 634—658. https://doi.org/10.1175/1520-0485(1998)028⟨0634:GSABIO⟩2.0.CO;2

Hofmeister, R., Burchard, H., Beckers, J-M., 2010. Non-uniform adaptive vertical grids for 3D numerical ocean models. Ocean Model. 33 (1—2), 70—86. https://doi.org/10.1016/j.ocemod.2009.12.003

Hoskins, B.J., 1974. The role of potential vorticity in symmetric stability and instability. Q. J. R. Met. Soc. 100, 480—482.

Hoskins, B.J., 1982. The mathematical theory of frontogenesis. Annu. Rev. Fluid Mech. 82, 131—151. https://doi.org/10.1146/annurev.fl.14.010182.001023

Hoskins, B.J., Bretherton, F.P., 1972. Atmospheric frontogenesis models: mathematical formulation and solution. J. Atmos. Sci. 29, 11—37. https://doi.org/10.1175/1520-0469(1972)029⟨0011:AFMMA⟩2.0.CO;2

Jing, Z., Fox-Kemper, B., Cao, H., Zheng, R., Du, Y., 2021. Submesoscale fronts and their dynamical processes associated with symmetric instability in the Northwest Pacific Subtropical Ocean. J. Phys. Oceanogr. 51, 83—100. https://doi.org/10.1175/JPO-D-20-0076.1

Johansson, J., 2018. Total and regional runoff to the Baltic Sea, HELCOM Baltic Sea Environment Fact Sheets. Online. 20.12.2018. http://www.helcom.fi/baltic-sea-trends/environment-fact-sheets/

Kalda, J., Soomere, T., Giudici, A., 2014. On the finite-time compressibility of the surface currents in the Gulf of Finland, the Baltic Sea. J. Mar. Syst. 129, 56—65. https://doi.org/10.1016/j.jmarsys.2012.08.010

Karimova, S.S., Lavrova, O.Yu., Solov'ev, D.M., 2012. Observation of Eddy Structures in the Baltic Sea with the Use of Radiolocation and Radiometric Satellite Data. Izvestiya, Atmos. Ocean. Phys. 48 (9), 1006—1013. https://doi.org/10.1134/S0001433812090071

Klingbeil, K., Mohammadi-Aragh, M., Gräwe, U., Burchard, H., 2014. Quantification of spurious dissipation and mixing — discrete variance decay in a finite-volume Framework. Ocean Model. 81, 49—64. https://doi.org/10.1016/j.ocemod.2014.06.001

Klingbeil, K., Lemarié, F., Debreu, L., Burchard, H., 2018. The numerics of hydrostatic structured-grid coastal ocean models: State of the art and future perspectives. Ocean Model. 125, 80—105. https://doi.org/10.1016/j.ocemod.2018.01.007

Krauss, W., Brügge, B., 1991. Wind-produced water exchange between the deep basins of the Baltic Sea. J. Phys. Oceanogr. 21, 373—384. https://doi.org/10.1175/1520-0485(1991)021⟨0373:WPWEBT⟩2.0.CO;2

Kuzmina, N.P., 1981. Non-linear numerical model of oceanic frontogenesis. Izvestiya Akademii Nauk SSSR Fizika Atmosfery i Okeana 17 (12), 1318—1325.

Kuzmina, N.P., Rodionov, V.B., 1992. Influence of baroclinity on the formation of thermohaline intrusions in ocean frontal zones. Izv. Akad. Sci. USSR, Atmos. Ocean. Phys. 28, 804—810.

Kuzmina, N.P., Rudels, B., Stipa, T., Zhurbas, V., 2005. The structure and driving mechanisms of the Baltic intrusions. J. Phys. Oceanogr. 35, 1120—1137. https://doi.org/10.1175/JPO2749.1

Kuzmina, N.P., Zhurbas, V.M., 2000. Effects of double diffusion and turbulence on interleaving at baroclinic oceanic fronts. J. Phys. Oceanogr. 30 (12), 3025—3038. https://doi.org/10.1175/1520-0485(2000)030⟨3025:EODDAT⟩2.0.CO;2

Laanemets, J., Väli, G., Zhurbas, V., Elken, J., Lips, I., Lips, U., 2011. Simulation of mesoscale structures and nutrient transport during summer upwelling events in the Gulf of Finland in 2006. Boreal Environ. Res. 16 (A), 15—26.

Lappe, C., Umlauf, L., 2016. Efficient boundary mixing due to near-inertial waves in a nontidal basin: Observations from the Baltic Sea. J. Geophys. Res.- Oceans 121 (11), 8287—8304. https://doi.org/10.1002/2016JC011985

Liblik, T., Väli, G., Lips, I., Lilover, M.-J., Kikas, V., Laanemets, J., 2020. The winter stratification phenomenon and its consequences in the Gulf of Finland. Baltic Sea, Ocean Sci. 16, 1475—1490. https://doi.org/10.5194/os-16-1475-2020

Lips, U., Zhurbas, V., Skudra, M., Väli, G., 2016. A numerical study of circulation in the Gulf of Riga, Baltic Sea. Part I: Whole-basin gyres and mean currents. Cont. Shelf Res. 112, 1—13. https://doi.org/10.1016/j.csr.2015.11.008

Männik, A., Merilain, M., 2007. Verification of different precipitation forecasts during extended winter-season in Estonia. HIRLAM Newsletter 52, 65—70.

MacVean, M.K., Woods, J.D., 1980. Redistribution of scalars during upper oceanfrontogenesis. Quart. J. Roy. Met. Soc. 106, 293—311.

Martinsen, E.A., Engedahl, H., 1987. Implementation and testing of a lateral boundary scheme as an open boundary condition in a barotropic ocean model. Coast. Eng. 11, 603—627. https://doi.org/10.1016/0378-3839(87)90028-7

May, B.D., Kelley, D.E., 1997. Effect of baroclinicity on double-diffusive interleaving. J. Phys. Oceanogr. 27, 1997—2008. https://doi.org/10.1175/1520-0485(1997)027⟨1997:EOBODD⟩2.0.CO;2

McIntyre, E., 1970. Diffusive destabilization of the baroclinic circular vortex. Geophys. Fluid Dynam. 1, 19—57.

McWilliams, J.C., 2016. Submesoscale currents in the ocean. Proc. Royal Soc. A 72, 20160117. https://doi.org/10.1098/rspa.2016.0117

Munk, W., 2001. Spirals on the sea. Scientia Mar 65 (S2), 193—198. https://doi.org/10.3989/scimar.2001.65s2193

Munk, W., Armi, L., Fischer, K., Zachariasen, F., 2000. Spirals on the sea. Proc. R. Soc. Lond A456, 1217—1280.

Onken, R., Baschek, B., Angel-Benavides, I.M., 2020. Very high-resolution modelling of submesoscale turbulent patterns and processes in the Baltic Sea. Ocean Sci. 16, 657—684. https://doi.org/10.5194/os-16-657

Ooyama, K., 1966. On the stability of the baroclinic circular vortex: a sufficient criterion for instability. J. Atmos. Sci. 23, 43—53. https://doi.org/10.1175/1520-0469(1966)023⟨0043:OTSOTB⟩2.0.CO;2

Ou, H.W., 1984. Geostrophic adjustment: a mechanism for frontogenesis. J. Phys. Oceanogr. 14, 994—1000. https://doi.org/10.1175/1520-0485(1984)014⟨0994:GAAMFF⟩2.0.CO;2

Qiu, B., Chen, S., Klein, P., Sasaki, H., Sasai, Y., 2014. Seasonal mesoscale and submesoscale eddy variability along the Nort Pacific Subtropical Countercurrent. J. Phys. Oceanogr. 44, 3079—3098. https://doi.org/10.1175/JPO-D-14-0071.1

Ruddick, B., 1992. Intrusive mixing in a Mediterranean salt lens - intrusion slopes and dynamical mechanisms. J. Phys. Oceanogr. 22 (11), 1274—1285. https://doi.org/10.1175/1520-0485(1992)022lt;1274:IMIAMS⟩2.0.CO;2

Shadden, S.C., Lekien, F., Marsden, J.E., 2005. Definition and properties of Lagrangian coherent structures from finite-time Lyapunov exponents in two-dimensional aperiodic flows. Physica D 212, 271—304. https://doi.org/10.1016/j.physd.2005.10.007

Schubert, R., Gula, J., Greatbatch, R.J., Baschek, B., Biastoch, A., 2020. The submesoscale kinetic energy cascade: Mesoscale absorption of submesoscale mixed layer eddies and frontal downscale fluxes. J. Phys. Oceanogr. 50, 2573—2589. https://doi.org/10.1175/JPO-D-19-0311.1

Smith, K.S., Ferrari, R., 2009. The production and dissipation of compensated thermohaline variance by mesoscale stirring. J. Phys. Oceanogr. 39, 2477—2501. https://doi.org/10.1175/2009JPO4103.1

Stern, M.E., 1967. Lateral mixing of water masses. Deep-Sea Res. 14, 747—753.

Stone, P.H., 1966. On non-geostrophic baroclinic stability. J. Atmos. Sci. 23 (4), 390—400.

Taylor, J.R., Ferrari, R., 2009. On the equilibration of a symmetrically unstable front via a secondary shear instability. J. Fluid Mech. 622, 103—113. https://doi.org/10.1017/S0022112008005272

Thomas, L.N., 2005. Destruction of potential vorticity by winds. J. Phys. Oceanogr. 35, 2457—2466. https://doi.org/10.1175/JPO2830.1

Thomas, L.N., Taylor, J.R., D'Asaro, E.A., Lee, C.M., Klymak, J.M., Shcherbina, A., 2016. Symmetric instability, inertial oscillations, and turbulence at the Gulf Stream front. J. Phys. Oceanogr. 46 (1), 197—217. https://doi.org/10.1175/JPO-D-15-0008.1

Thomas, L.N., Taylor, J.R., Ferrari, R., Joyce, T.M., 2013. Symmetric instability in the Gulf Stream. Deep-Sea Res. Part II 91, 96—110. https://doi.org/10.1016/j.dsr2.2013.02.025

Umlauf, L., Burchard, H., 2005. Second-order turbulence closure models for geophysical boundary layers. A review of recent work. Cont. Shelf Res. 25 (7—8), 795—827. https://doi.org/10.1016/j.csr.2004.08.004

Umlauf, L., Arneborg, L., 2009. Dynamics of rotating shallow gravity currents passing through a channel. Part I: Observation of transverse structure. J. Phys. Oceanogr. 39, 2385—2401. https://doi.org/10.1175/2009JPO4159.1

Väli, G., Zhurbas, V., 2021. Seasonality of submesoscale coherent vortices in the northern Baltic Proper: A model study. Fudamentalnaya i Prikladnaya Gidrofisika 14 (3) (in press).

Väli, G., Zhurbas, V.M., Laanemets, J., Lips, U., 2018. Clustering of floating particles due to submesoscale dynamics: a simulation study for the Gulf of Finland, Fundamentalnaya i prikladnaya gidrofizika 11(2), 21—35. https://doi.org/10.7868/S2073667318020028

Väli, G., Zhurbas, V., Lips, U., Laanemets, J., 2017. Submesoscale structures related to upwelling events in the Gulf of Finland, Baltic Sea (numerical experiments). J. Mar. Syst. 171 (SI), 31—42. https://doi.org/10.1016/j.jmarsys.2016.06.010

Vankevich, R.E., Sofina, E.V., Eremina, T.E., Ryabchenko, V.A., Molchanov, M.S., Isaev, A.V., 2016. Effects of lateral processes on the seasonal water stratification of the Gulf of Finland: 3-D NEMO-based model study. Ocean Sci. 12, 987—1001. https://doi.org/10.5194/os-12-987-2016

Villermaux, E., 2019. Mixing versus stirring. Annu. Rev. Fluid Mech. 51, 245—273. https://doi.org/10.1146/annurev-fluid-010518-040306

Vortmeyer-Kley, R., Holtermann, P.L., Feudel, U., Gräwe, U., 2019. Comparing Eulerian and Lagrangian eddy census for a tide-less, semi-enclosed basin, the Baltic Sea, Ocean Dyn. 69, 701—717. https://doi.org/10.1007/s10236-019-01269-z

Yu, X., Garabato, A.C.N., Martin, A.P., Buckingham, C.E., Brannigan, L., 2019. An annual cycle of submesoscale vertical flow and restratification in the upper ocean. J. Phys. Oceanogr. 49, 1439—1461. https://doi.org/10.1175/JPO-D-18-0253.1

Zhurbas, V., Elken, J., Paka, V., Piechura, J., Väli, G., Chubarenko, I., Golenko, N., Shchuka, S., 2012. Structure of unsteady overflow in the Słupsk Furrow of the Baltic Sea. J. Geophys. Res. Oceans 117, C04027. https://doi.org/10.1029/2011JC007284

Zhurbas, V., Laanemets, J., Vahtera, E., 2008. Modeling of the mesoscale structure of coupled upwelling/downwelling events and the related input of nutrients to the upper mixed layer in the Gulf of Finland, Baltic Sea. J. Geophys. Res. Oceans 113, C05004. https://doi.org/10.1029/2007JC004280

Zhurbas, V., Väli, G., Golenko, M., Paka, V., 2018. Variability of bottom friction velocity along the inflow water pathway in the Baltic Sea. J. Mar. Syst. 184, 50—58. https://doi.org/10.1016/j.jmarsys.2018.04.008

Zhurbas, V., Väli, G., Kostianoy, A., Lavrova, O., 2019a. Hindcast of the mesoscale eddy field in the Southeastern Baltic Sea: Model output vs satellite imagery. Russian J. Earth Sci. 19 (4), 1—17. https://doi.org/10.2205/2019ES000672

Zhurbas, V., Väli, G., Kuzmina, N., 2019b. Rotation of floating particles in submesoscale cyclonic and anticyclonic eddies: a model study for the southeastern Baltic Sea. Ocean Sci. 15, 1691—1705. https://doi.org/10.5194/os-15-1691-2019